

1 **Geophysical Trends inferred from 20 years of AIRS**  
2 **infrared global observations**

3 **S. DeSouza-Machado<sup>1</sup>, L. Larrabee Strow<sup>1,2</sup>, R. Kramer<sup>3</sup>**

4 <sup>1</sup>JCET/GESTAR2, University of Maryland Baltimore County, Baltimore, Maryland

5 <sup>2</sup>Dept of Physics, University of Maryland Baltimore County, Baltimore, Maryland

6 <sup>3</sup>NOAA GFDL, Princeton New Jersey

7 **Key Points:**

- 8 • The 20+ year low noise high spectral radiance record by NASA's Atmospheric In-  
9 frared Sounder contains detailed vertical information about surface and atmospheric  
10 temperature and water vapor.  
11 • Trends from the radiance measurements are analyzed in a novel way for long-term  
12 climate studies, different than traditional use of infrared radiances in daily retrievals  
13 or assimilation into Numerical Weather Prediction Models.

---

Corresponding author: Sergio DeSouza-Machado, [sergio@umbc.edu](mailto:sergio@umbc.edu)

## 14 Abstract

15 NASA's Atmospheric Infrared Sounder has been in near-continuous operation since  
 16 September 2002. The  $\sim 3$  million daily spectral observations contain detailed informa-  
 17 tion about surface and atmospheric temperature, water vapor and trace gases such as  
 18  $\text{CO}_2$  and  $\text{CH}_4$ , as well as clouds and aerosols. In this paper we obtain climate thermo-  
 19 dynamic trends using 20 years of AIRS observations by working exclusively with the trends  
 20 observed in the AIRS radiance time series. This is achieved by first binning the observed  
 21 spectra into nominal  $3 \times 5$  degree latitude/longitude spatial subsets using 16 day inter-  
 22 vals, after which a quantile-based algorithm selects nominally clear scenes for each grid  
 23 box in order to construct the clear scene radiance spectrum time series. De-seasonalized  
 24 spectral anomalies and spectral trends are then obtained from the time series, which are  
 25 converted into geophysical trends using a physical retrieval for each grid box. This approach  
 26 is completely different from traditional operational use of infrared data for trending, whereby  
 27 anomalies/trends are generated either after daily retrievals, or after assimilation into NWP  
 28 models. Our approach rigorously ties the derived geophysical trends to the observed ra-  
 29 diance trends, and requires orders-of-magnitude fewer computational resources and time  
 30 than re-analysis or traditional Level 2 retrievals. The retrieved trends are compared to  
 31 trends derived from four other products : ERA5, MERRA2 reanalysis model fields and  
 32 the NASA Level3 AIRS v7 and NASA Level 3 CLIMCAPS v2. Our retrieved surface tem-  
 33 perature trends agree quite well with ERA5 re-analysis, CLIMCAPS L3 and the GISS  
 34 surface climatology trends. Atmospheric temperature profile trends exhibit some vari-  
 35 ability amongst all these data sets, especially in the polar stratosphere. Water vapor pro-  
 36 file trends are nominally similar amongst all data sets except for the AIRS v7 which ex-  
 37 hibits trends with a different sign in the mid troposphere. ~~Note that infrared sounders~~  
 38 ~~lose water vapor sensitivity close to the surface making intercomparisons of column water~~  
 39 ~~trends problematic.~~ Spectral closure between observation trends versus those computed  
 40 by running all the NWP re-analysis and official NASA L3 monthly fields though a (clear  
 41 sky) radiative transfer code is discussed, with the major differences arising in the wa-  
 42 ter vapor sounding region.

## 43 Plain Language Summary

44 The new generation of infrared sounders, designed for weather forecasting purposes,  
 45 have been in orbit around the Earth for a long enough time to enable anomaly and trending  
 46 studies for climate purposes. Traditionally their daily obtained radiance data has been  
 47 used for operational atmospheric state retrievals, or assimilation into Numerical Weather  
 48 Prediction models, after which climate anomaly studies are made. In this paper we use  
 49 the raw radiance spectral data to form radiance anomalies and trends, after which we  
 50 do a one step atmospheric state retrieval. This novel approach has the benefit of using  
 51 only stable channels together with easily understood assumptions and well tested retrieval  
 52 algorithms to do the trend or anomaly geophysical retrieval, which has full error characterization.  
 53

## 54 1 Introduction

55 NASA's Atmospheric Infrared Sounder (AIRS) became operational in September  
 56 2002, as the first of the new generation of low noise, high stability hyperspectral sounders,  
 57 making Top of Atmosphere (TOA) radiance observations at a typical 15km (at nadir)  
 58 horizontal resolution. Follow on instruments with similar characteristics and abilities in-  
 59 clude Eumetsat's Infrared Atmospheric Sounding Interferometer (IASI) and NOAA's Cross  
 60 Track Infrared Sounder (CrIS), operational since June 2007 and March 2012 respectively.  
 61 The latter two already have follow on missions planned till the 2040s, and together these  
 62 three sounders will provide scientists with a 40 year high quality, near continuous ob-  
 63 servational dataset for climate anomaly and trending studies.

64 Infrared radiances contain a wealth of information, including but not limited to sur-  
 65 face temperature, atmospheric temperature and water amount, and mixing ratios of green-  
 66 house gases such as carbon dioxide CO<sub>2</sub>, CH<sub>4</sub> and N<sub>2</sub>O. Measurements by visible imagers  
 67 which have ~ 1 km horizontal resolution or better King et al. (2013) suggest global cloud  
 68 free fractions of ~ 30%, but the 15 km footprint of typical sounders means at most 5%  
 69 of the hyperspectral observations can be considered “cloud-free.” Current operational NASA  
 70 L2 products ~~come from cloud clearing the observed radiances, which introduces errors~~  
 71 ~~and use the method of cloud clearing on observed radiances in partly cloudy scene conditions~~  
 72 ~~before doing the geophysical retrieval. The cloud clearing method solves for an estimate~~  
 73 ~~of clear column radiances by examining adjacent Fields of View (FOVs) to estimate the~~  
 74 ~~cloud effects on observed allsky radiances, assuming any differences are solely due to different~~  
 75 ~~cloud amounts in each FOV, and significantly increases geophysical retrieval yields (to~~  
 76 ~~about 50-60%) Smith and Barnet (2023). This does introduce increased noise in the cloud~~  
 77 ~~cleared radiances of the lower atmosphere sounding channels; in addition the subsequent~~  
 78 ~~retrieval depends on the first guess (which is a neural net for AIRS v7 and MERRA2 re-~~  
 79 ~~analysis for CLIMCAPS v2). The reader is referred to Susskind et al. (2003); Smith and Barnet (2020)~~  
 80 ~~Susskind et al. (2003); Smith and Barnet (2020, 2023) for more details.~~

81 In this paper we work directly in radiance space and form either anomalies or trends  
 82 from the underlying well characterized and understood radiances Strow and DeSouza-  
 83 Machado (2020), in order to do a geophysical trend or anomaly retrieval. The work pre-  
 84 sented here, once the averaged/sorted data is available, can be processed in hours to days,  
 85 and can be duplicated by small research groups with ease. Moreover, our novel approach  
 86 has zero temperature *a-priori* and minimal water vapor *a-priori*. This completely sidesteps  
 87 time variability and the accuracy of the *a-priori* which causes errors in the retrievals,  
 88 and ensures our work examines trends directly inferred from the radiances versus those  
 89 from traditional methods, ~~leading-~~ This leads to more unbiased results that directly high-  
 90 light the conditions (for example stratospheric water vapor) where the sensor has lim-  
 91 ited sensitivity.

92 The approaches used in this work are therefore very different than climate anoma-  
 93 lies or trends from reanalysis products or traditional Level 2 retrievals, neither of which  
 94 are tailored for climate trends. Reanalysis ~~uses a wide range of observations and are only~~  
 95 ~~created within very large organizations, and represent the most commonly used climate~~  
 96 ~~data sets. They products~~ assimilate individual sensor scenes from many different instruments,  
 97 and may have discontinuities as different instruments come online or go offline. Tradi-  
 98 tional Level 2 (and Level 3 products derived from Level 2) retrieve the atmospheric state  
 99 for individual scenes (or effective cloud-cleared radiance derived from a 3x3 grid of in-  
 100 dividual scenes). Both reanalysis and Level 2 products require large computational re-  
 101 sources, that preclude full dataset re-processing to help fully understand trends. A main  
 102 characteristic of traditional L2 retrievals is the requirement for a good *a-priori* state for  
 103 each inversion, making errors in the *a-priori* difficult to distinguish from true variabil-  
 104 ity in the data, especially with regard to trends.

105 The stability and accuracy of the AIRS instrument is documented in recent work  
 106 on analyzing 16 years of AIRS radiance anomalies over cloud-free ocean Strow and DeSouza-  
 107 Machado (2020). Geophysical retrievals on the anomalies yielded CO<sub>2</sub>, CH<sub>4</sub>, N<sub>2</sub>O and  
 108 surface temperature time series that compared well against in-situ data from NOAA Global  
 109 Monitoring Laboratories (GML) trace gas measurements and NOAA Goddard Institute  
 110 of Space Studies (GISS) surface temperature data respectively. A significant difference  
 111 between this paper and Strow and DeSouza-Machado (2020) is the nominally clear scenes  
 112 used in this paper are selected uniformly from all over the Earth, while the clear scenes  
 113 in the latter were zonal averages which were sometimes concentrated in certain regions.

114 In this paper we expand upon our initial zonal clear sky analysis, to derive geophys-  
 115 ical trends from 20 years (September 2002 - August 2022) of AIRS measurements over  
 116 ~ 3 × 5 degree tiles covering the Earth, chosen such that the number of observations

117 in each tile is roughly equal. An important concept introduced is spectral closure, whereby  
 118 the observed clear sky spectral radiance trends are compared to spectral trends produced  
 119 by running the monthly reanalysis or official NASA retrieved AIRS L3 products through  
 120 an accurate clear sky radiative transfer code; close agreement in different sounding re-  
 121 gions (such as 640-800  $\text{cm}^{-1}$  for temperature and  $\text{CO}_2$ , 1350-1640  $\text{cm}^{-1}$  for water va-  
 122 por, 1000-1150  $\text{cm}^{-1}$  for  $\text{O}_3$ ) between the computed and actual observed spectral trends  
 123 imply that trends from those geophysical parameters used in the computations are re-  
 124 alistic while disagreement suggests otherwise. A companion paper will utilize the geo-  
 125 physical trend results to derive Outgoing Longwave Radiation (OLR) trends and non-  
 126 local clearsky feedback parameters. Nominally clear scenes for each tile are picked out  
 127 using a quantile approach; from the time series, radiances trends are made over the en-  
 128 tire Earth, from which geophysical trends are retrieved.

129 Observed infrared spectral trends from AIRS has already been a focus of earlier  
 130 work by Huang et al. (2023) who studied a slightly shorter time period (2002-2020) while  
 131 Raghuraman et al. (2023) converted the radiances to Outgoing Longwave radiation (OLR),  
 132 but neither study involve retrievals from spectral trends to geophysical trends. Instead  
 133 they convert various model trends (such as ERA5) to spectral trends and compare against  
 134 the observed spectral trends. Our earlier work shows we can accurately account for the  
 135 effects of GHG forcings (Strow et al., 2021). In this paper we remove these GHG forc-  
 136 ings from the observed AIRS spectral trends to concentrate on atmospheric temperature  
 137 and water vapor and surface temperature, while the papers by Huang et al. (2023); Raghu-  
 138 raman et al. (2023) include the GHG forcings in the model generated spectral trends.  
 139 Another noteworthy examination of the time evolution of high spectral resolution infrared  
 140 radiances (converted to spectral outgoing longwave radiation (OLR) fluxes) by (Whitburn  
 141 et al., 2021) covered 10 years (2007-2017) of IASI observations. They confirmed that the  
 142 IASI-derived fluxes agreed well with increases in GHG gas concentrations and El-Nino  
 143 Southern Oscillation (ENSO) events within that time frame. A more recent paper Roemer  
 144 et al. (2023) used the 10 year IASI data to derive allsky longwave feedback spectral com-  
 145 ponents (water vapor,  $\text{CO}_2$ , window, ozone) and total values, while also estimating clear  
 146 sky feedback values.

147 We will refer to our results as the AIRS Radiance Trends (AIRS\_RT). Compar-  
 148 isons are made against monthly output from the European Center for Medium Weather  
 149 Forecast fifth generation reanalysis (ERA5) Hersbach et al. (2020) and NASA’s second  
 150 generation Modern-Era Retrospective analysis for Research and Applications (MERRA2)  
 151 Gelaro and Coauthors (2017), and also against the official monthly AIRS L3 products  
 152 which are AIRS v7 L3 Susskind et al. (2014); Tian et al. (2020) and CLIMCAPS v2 L3  
 153 Smith and Barnett (2019, 2020). Detailed geophysical trends and spectral closure stud-  
 154 ies are presented for the ascending (daytime (D)), descending (nighttime (N)) and D/N  
 155 averages.

## 156 2 Datasets used in this study

157 Three main types of datasets are used in this study. The first is the AIRS L1C ra-  
 158 diance dataset we analyzed for this paper, which has both daytime (D) and nighttime (N)  
 159 (ascending and descending) views of the planet. Second is the monthly operational L3  
 160 retrieval data, which are the AIRS v7 and the CLIMCAPS v2 products, also separated  
 161 into D/N data. Finally we also compared to trends from ERA5 and MERRA2 monthly  
 162 reanalysis model fields. The ERA5 monthly dataset is available in 8 averaged time steps,  
 163 so we match to the average AIRS overpass times and compute (D/N) data over the 20  
 164 years, while MERRA2 monthly model fields are only available as one time step; included  
 165 here for completeness we mention the NASA GISS surface temperature dataset, which  
 166 like MERRA2 is only available as ~~one set per month~~ a monthly mean. This means four  
 167 of the datasets : AIRS\_RT (from AIRS L1C), AIRS L3 and CLIMCAPS L3, and ERA5  
 168 are separable into D/N, while the other two (MERRA2 and GISS) are only available as

169 a diurnal averaged value. We describe these datasets in more detail below. ~~In addition~~  
 170 ~~we also briefly mention other datasets that we use.~~

## 171 2.1 The AIRS instrument and L1C dataset

172 The Atmospheric Infrared Sounder (AIRS) on board NASA’s polar orbiting EOS/Aqua  
 173 platform has 2378 channels, covering the Thermal Infrared (TIR) spectral range (roughly  
 174  $649\text{-}1613\text{ cm}^{-1}$ ) and shortwave infrared ( $2181\text{-}2665\text{ cm}^{-1}$ ). The full widths at half max-  
 175 imum satisfy  $\nu/\delta\nu \sim 1200$ . The (spectral dependent) noise is typically  $\leq 0.2\text{K}$ . The orig-  
 176 inal L1b radiance dataset suffers from spectral gaps and noise contaminated data as de-  
 177 tectors slowly fail. These limitations are addressed using a 2645 L1c channel dataset, where  
 178 spectral gaps and some of the noise “pops” are filled in using principal component recon-  
 179 struction Manning et al. (2020) and is the dataset used to subset radiances analyzed in  
 180 this paper. However we note that the results described in this paper used only the ac-  
 181 tual observed radiances in pristine, stable channels described in Strow et al. (2021) and  
 182 none of the synthetic channels. The Aqua platform is a polar orbiting satellite with 1.30  
 183 am descending (night time over equator) and 1.30 pm ascending (daytime over equator)  
 184 tracks. Each orbit takes about 90 minutes, with the 16 passes yielding almost twice daily  
 185 coverage of the entire planet. About  $\sim 3$  million AIRS spectral observations have been  
 186 obtained daily since AIRS became operational in late August 2002. The instrument has  
 187 provided data almost continuously since then though there have been some shutdowns  
 188 (each spanning a few days) such as during solar flare events.

189 In this paper we use the re-calibrated 2645 channel L1C radiance data Strow and  
 190 DeSouza-Machado (2020) instead of the 2378 L1B data. 20 years (spanning September  
 191 1, 2002-August 31, 2022) of AIRS L1C radiance data is gridded into 4608 tiles covering  
 192 the Earth : 72 longitude boxes which are all  $5^\circ$  in width, and 64 latitude boxes which are  
 193 approximately  $2.5^\circ$  in width at the tropics but wider at the poles to keep the number of  
 194 observations per 16 day intervals (which is the repeat cycle of the AIRS orbit on the Aqua  
 195 satellite) roughly the same. This way there are  $\sim 12000$  observations per 16 days per tile,  
 196 which are roughly equally divided between the ascending/daytime (D) and descending/nigh-  
 197 time (N) tracks. In this paper we discuss results for both the ascending and descending  
 198 tracks using a retrieval based on the longwave (LW) and midwave (MW) regions of the  
 199 spectrum ( $640\text{-}1620\text{ cm}^{-1}$  or  $6\text{-}15\text{ }\mu\text{m}$ ).

200 In this paper our trend retrievals use only the AIRS channels are stable in time,  
 201 as quantified in Strow et al. (2021). For example the shortwave (SW) channels are drift-  
 202 ing at a higher rate than the LW/MW channels, which can lead to incorrect surface tem-  
 203 perature rates, and are avoided in this paper. Similarly there are many channels in  
 204 the LW and MW whose detectors are drifting in time, and which are also not used here.  
 205 For example there are some higher wavenumber (shorter wavelength) channels past the  
 206 ozone band which have a significant drift in time, possibly due to changes in the polar-  
 207 ization of the scan mirror coating with time. Therefore compared to other AIRS oper-  
 208 ational products used in this paper, our results use channels that are demonstrated to  
 209 have high stability Strow et al. (2021). We do note that some of the observed drifts in  
 210 the AIRS channels stabilized after 6 years, so their impact is reduced when looking at  
 211 20 year trends.

212 ~~In “clear sky” scenes, the window region would be dominated by the effects of water~~  
 213 ~~vapor continuum absorption, which is largest for hot and humid tropical scenes and almost~~  
 214 ~~negligible for cold, dry scenes. Scattering and absorption by liquid and ice clouds also~~  
 215 ~~affects the window region (800-1000 and 1100-1250 , and 2400-2800 ). For each tile, we~~  
 216 ~~use the 1231.3 observation as our window channel (AIRS L1C channel ID = 1520), and~~  
 217 ~~form the quantiles of the observed Brightness Temperature (BT) for each 16 day observation~~  
 218 ~~period. BT 1231 therefore serves as a measure for the cloudiness of an observation : if~~  
 219 ~~there are no or low clouds, it will effectively measure the surface temperature, but as the~~

~~clouds get thicker and higher, it will measure colder temperatures. Quantiles 0.50, 0.80, 0.90, 0.95 and 0.97 were among those chosen; the first would be considered the “median” observation, containing clear and cloudy scenes. In a subsequent section we show Q0.90 onwards can be considered “almost free of clouds.” Our retrievals using this dataset are referred to as in what follows.~~

## 2.2 Reanalysis Model fields

The ERA5 fifth generation reanalysis product from the European Center for Medium Range Weather Forecasts is freely available on monthly timescales from the Copernicus Climate Data Store. This monthly dataset is output at 37 pressure levels at  $0.25^\circ$  horizontal resolution Hersbach et al. (2020), which is further subdivided into eight 3-hour averages per month (corresponding to 00,03,06,...21 UTC). For each month from September 2002-August 2022 we downloaded the surface temperature and pressure fields, as well as atmospheric temperature, water vapor and ozone fields. These are then colocated to each tile center using 2D spatial interpolation, as well as time interpolated according to the average AIRS overpass time as a function of month. From the resulting monthly time-series of reanalysis model fields for each tile, we generated (a) thermodynamic trends for surface temperature, air temperature, water vapor and ozone model fields (b) a 20 year average thermodynamic profile in order to produce jacobians for the linear trend retrievals (c) by using the model fields as input to the clear sky SARTA radiative transfer code Strow, Hannon, DeSouza-Machado, et al. (2003) a monthly time series of clear sky radiances for each tile was generated, from which we could compute radiance trends. We did this for both the ascending and descending datasets.

The MERRA version 2 (MERRA2) re-analysis used in this paper is the second generation Gelaro and Coauthors (2017) product from NASA’s Global Modeling and Assimilation Office. The monthly data we use is available on 42 pressure levels at a horizontal resolution of  $0.5^\circ \times 0.625^\circ$ , but only one monthly mean diurnally averaged output is available per month. Similar to the ERA5 output, we colocated the MERRA2 surface temperature, atmospheric temperature, water vapor and ozone fields to our tile centers for each month starting September 2002 in order to produce a time series of radiance and model output, from which radiance and thermodynamic trends could be computed for comparisons against other datasets in this study; similar to above we also generated a monthly time series of clear sky radiances for each tile, from which we could compute clear sky radiance trends based on MERRA2.

The NASA Goddard Institute of Space Studies (GISS) surface temperature data v4 surface temperature data 2023 (2005); Lenssen et al. (2019) is a monthly dataset based primarily on near surface temperatures land stations, and data from ships and buoys. As with MERRA2 we obtained one monthly mean dataset per month, which we could not separate into descending (N) or ascending (D) tracks.

## 2.3 AIRS L3 Products

NASA routinely produces two retrievals from the AIRS L1C data observed each day, which are AIRS v7 Susskind et al. (2014); Tian et al. (2020) and CLIMCAPS v2 Smith and Barnett (2019, 2020). Both use the cloud clearing process but there are significant algorithmic differences; in particular the AIRS v7 product is initialized by a neural net, while CLIMCAPS uses MERRA2 for its initialization. The L2 products are then individually turned into L3 monthly products, for both the ascending (daytime) and descending (nighttime) data. The timeseries of thermodynamic profiles were used as input to the clear sky SARTA RTA to generate radiances, after which radiance trends and thermodynamic trends are also produced.

268

## 2.4 Other L3 Products

269

270

271

272

The Microwave Limb Sounder (MLS) monthly binned water vapor (H<sub>2</sub>O) mixing ratio dataset Lambert et al. (2021), which contains data at spatial coverage  $\pm 82^\circ$  latitude, at a spatial resolution of  $4^\circ \times 5^\circ$  and useful vertical range between 316 and 0.00215 hPa was used in this paper to improve retrieval trends in the upper atmosphere.

273

## 3 Filtering the Observational Data for clear scenes

274

275

276

277

278

279

280

Here we discuss the “clear scene” selection from all the observed data stored for each of the  $72 \times 64$  tiles. Ideally we would prefer to use a MODIS cloud fraction product (1 km) colocated to the 15 km AIRS footprints, but this is presently unavailable. Our earlier work used an uniform clear flag over ocean Strow et al. (2021) which will not work well over land because of surface inhomogeneity. In this section we discuss an alternative clear filter based on the hottest 10 percent of AIRS observations that are present inside any 16 day tile, over any location.

281

### 3.1 Observed BT1231 Distributions

282

283

284

285

286

287

288

289

290

291

292

293

294

295

296

297

298

299

300

The ~~left panel of~~ radiances measured in thermal infrared window region ( $800\text{--}1000\text{ cm}^{-1}$  and  $1100\text{--}1250\text{ cm}^{-1}$ ) are dominated by the effects of the surface temperature, water vapor continuum absorption and cloud/aerosol effects. The effects of water vapor continuum absorption is largest in hot and humid tropical scenes (depressing the observations relative to surface temperatures by about 5-6 K, which reduces to about 2 K at  $\pm 50^\circ$ ) and is almost negligible for cold, dry scenes (less than 1 K). Scattering and absorption by liquid and ice clouds also affects the window region (Deep Convective Clouds can depress the window channel observations by as much as 100 K relative to surface temperatures). For each tile, we use the  $1231.3\text{ cm}^{-1}$  observation as our representative window channel (AIRS LIC channel ID = 1520), as it is minimally impacted by weak water vapor lines. Changed to Brightness temperature (BT) the observation in this  $1231.3\text{ cm}^{-1}$  channel (BT1231) therefore serves as a measure for the cloudiness of an observation: if there are no or low or optically thin clouds, it will effectively measure the surface temperature, but as the clouds get thicker and higher, it will measure the cold cloud top temperatures. For any tile during any 16 day observation periods, we can compute quantiles  $Q$  based on the observed BT1231 to screen between cloudy and partially clear scenes. We chose different BT1231 quantiles (so quantile  $Q_{0.XY}$  will have a numerical value  $BT_{1231,Q_{0.XY}}$  associated with it) and show below the data contained between  $Q_{0.90}$  and  $Q_{1.00}$  can be considered “almost free of clouds.”

301

302

303

304

305

306

307

308

309

310

311

312

313

314

315

316

317

Figure 1 shows ~~the zonally averaged histograms for a~~ all the BT1231 observations for a chosen 16 day timestep in the form of a zonally averaged histogram (normalized probability distribution functions (PDFs)), with latitude on the vertical axis and BT1231 on the horizontal axis. The colorbar is the PDF value, and we used data spanning August 27, 2012 - September 11, 2012 which is approximately half way through the 20 year AIRS mission dataset used in this paper. ~~The colorbar is the mean histogram (normalized probability distribution functions (PDFs)) using the data in that 16 day time period. From this we plot the curves show the~~ zonally averaged BT1231 values of the minimum ( $Q_{0.00}$ ) in dark cyan, mean (thick red), ~~mean,~~ median ( $Q_{0.50}$ ) in orange, maximum ( $Q_{1.00}$ ) in light cyan; also shown are ~~the a handful of other~~ zonally averaged BT1231 values of  $Q_{0.80}$ ,  $Q_{0.90}$ , for example  $Q_{0.80}$ ,  $Q_{0.90}$  (thick black curve),  $Q_{0.95}$  and  $Q_{0.97}$ . The BT1231 channel has the lowest expected absorption due to water vapor in the longwave portion of the spectrum, and so is expected to sense the surface temperature unless the scene is cloudy in which case it would be expected to sense the cloud top temperature. In this way the histogram should exhibit the characteristics of the cloud conditions observed in the 16 day period.  $Q_{0.95}$  and  $Q_{0.97}$ . The distributions are skewed to the left (negative skewness), as confirmed by the mean being less than the median. We also point out that

even  $Q_{0.80}$  sees much of the surface from the southern tropics to the northern polar region. The 220 K horizontal axis cutoff means we do not see the very cold (190 K) observations over the winter Antarctic.

The figure shows the expected qualitative features, for example (1) the tropical PDFs peak at around 295 K, but show some warmer observations, as well much colder observations (below 230 K) corresponding to Deep Convective Clouds (DCC); this gives a dynamic range of almost 100 K at the tropics (2) the BT1231 observed over the Southern Polar (polar winter) regions are much colder than the BT1231 observed over the Northern Polar (polar summer) regions and (3) the reddish peaks in the 30°N - 40°N are a combination of the marine boundary layer (MBL) clouds and warmer summer land temperatures.

It is evident the distributions are skewed to the left (negative skewness), as confirmed by the mean being less than the median. We also point out that even  $Q_{0.80}$  sees much of the surface from the southern tropics to the northern polar region. The right panel of Figure 1 shows the same information, except presented as a cumulative histogram, with a value of 0 at the hot end (340 K) and 1 at the cold end (180 K); again one sees the  $Q_{0.90}$  quantile envelopes the hottest 10% of the observations as expected. The cutoff of 220 K in the plots does not allow the plot to extend to show the very cold (190 K) observations over the winter Antarctic.

Zonally averaged BT1231 histograms for an 2012/08/27 - 2012/09/11 timespan (colorbar) and quantiles (curves). The thick black curve is the  $Q_{0.90}$  quantile (and above) used in this paper, and is very close to the maximum. The left hand panel shows the normalized histogram (probability distribution function) as a function of latitude and temperature bin; the right hand panel shows the cumulative distribution function, though starting from the hotter side ( $\text{cdf}(340 \text{ K}) = 0.0$ ,  $\text{cdf}(180 \text{ K}) = 1.0$ ).

Measurements by visible imagers which have  $\sim 1$  km horizontal resolution or better King et al. (2013) suggest global cloud free fractions of  $\sim 30\%$ , but the 15 km footprint of typical sounders means at most 5% of the hyperspectral observations can be considered “cloud free.” In the tropics, the higher amounts of water vapor means the observed BT1231 for a clear scene would be reduced by a 5-6 K due to water vapor continuum (which on average reduces to about 2 K at  $\pm 50$ , and 1 K at the polar regions). Figure 1 shows on average the on average the cloud effect at the tropics is an additional modest 20 K (difference between  $Q_{0.90}$  and  $Q_{0.50}$   $Q_{0.90}$  and  $Q_{0.50}$ ) compared to the 100 K dynamic range. This is because the cloud fractions and cloud decks in the individual observations have effectively more clouds (with larger cloud fraction in the FOV) lower in the atmosphere than higher up; the net effect is that in the window region the atmosphere is on average radiating from the lower (warmer) altitudes, and so  $Q_{0.80}$  to  $Q_{1.00}$  onwards spectra whose BT1231 values are larger than  $BT_{1231, Q_{0.80}}$ , see much of the surface emission as well.

We now use the above plots to select “almost clear” scenes. For any one tile, we define set  $\Psi_{0,XY}$  to have all observations  $i$  whose BT1231 lies between quantiles  $Q_{0,XY}$  and  $Q_{1,00}$ ,  $\{i \mid BT_{1231, Q_{0,XY}} \leq BT_{1231}(i) \leq BT_{1231, Q_{1,00}}\}$ . In what follows in this subsection we use an “integrated” or “cumulative” quantile wherein  $Q_{0.90}$  now means all scenes between  $Q_{0.90}$  and  $Q_{1.00}$  (maximum observed BT) are considered.  $XY$  is the radiances averaged over all the observations  $i$  which are in the set  $\Psi_{0,XY}$ , namely

$$r_{Q_{0,XY}}(\nu) = \frac{1}{N_{0,XY}} \sum_{i \in \Psi_{0,XY}} r_i(\nu) \quad (1)$$



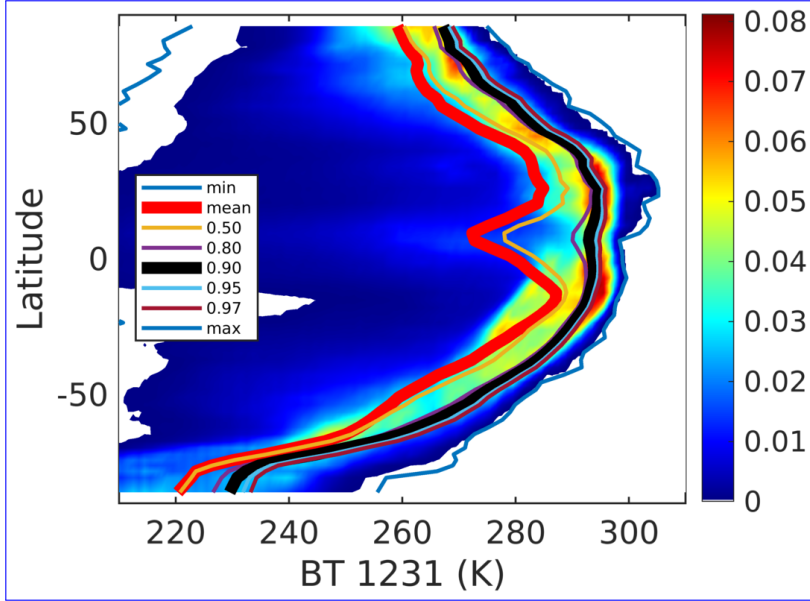


**Figure 1.** Zonally averaged BT1231 normalized histograms (probability distribution functions) as a function of latitude and temperature bin, for an 2012/08/27 - 2012/09/11 timespan (colorbar) and quantiles (curves). The thick black curve is the Q0.90 quantile (and above) used in this paper, and is very close to the maximum Q1.00 quantile.

364 where  $r_i(\nu)$  are the  $N_{0,XY}$  individual observations in set  $\Psi_{0,XY}$ . In this section we only  
 365 use the  $\nu = 1231 \text{ cm}^{-1}$  channel, but in later sections we easily form averages for all 2645  
 366 channels, at any 16 day time step for any tile.

367 ~~To further investigate if the scenes chosen using this definition can be considered~~  
 368 ~~We tested different quantile sets  $\Psi_{0,XY}$  to see which one can reliably be considered~~  
 369 ~~to provide a nominally “cloud free” ~~we compare to global dataset~~, and chose the Q0.90 average~~  
 370 ~~(ie defined as averaged over the  $\Psi_{0.90}$  set) as the one to use for the rest of this paper,~~  
 371 ~~unless explicitly stated otherwise. The tests primarily involved comparisons to scenes~~  
 372 ~~produced by the uniform/clear sky filter described in Strow and DeSouza-Machado (2020)~~  
 373 ~~for the same August 27, 2012 - September 11, 2012 sixteen day timespan. This latter fil-~~  
 374 ~~ter selects clear scenes by both testing for uniformity (to within 0.5 K) across a  $3 \times 3$~~   
 375 ~~grouping of AIRS scenes and also using a criteria that the observed window channel ob-~~  
 376 ~~servations should be within  $\pm 4$  K of clear-sky simulations using thermodynamic param-~~  
 377 ~~eters supplied by ~~reanalysis-reanalysis~~ models. The results are shown in the left hand plot~~  
 378 ~~of Figure 2, plotted on a  $1^\circ \times 1^\circ$  grid. We note in this plot the uniform/clear scenes that~~  
 379 ~~are plotted are limited to those over ocean, and for solar zenith less than  $90^\circ$  (daytime),~~  
 380 ~~which automatically filtered out many of the views over the (wintertime) Southern Po-~~  
 381 ~~lar region. Immediately apparent are the gaps produced by the uniform/clear filter *e.g.*~~  
 382 ~~in the Tropical West Pacific or off the western coasts of continents where there are clouds.~~  
 383 ~~The gaps can be changed by *e.g.* changing the 4K threshold to allow more or fewer scenes~~  
 384 ~~through the filter.~~

385 ~~The center plot shows the scenes selected by the integrated for all tiles, the daytime~~  
 386 ~~scenes selected for the Q0.90 filter average for the same time period, on the same  $1^\circ \times$~~   
 387  ~~$1^\circ$  grid. Compared to the left hand plot, the spatial coverage is almost complete, as the~~  
 388 ~~Q0.90 filter average always has the hottest 10% of the observations, the spatial coverage~~  
 389 ~~is almost complete: gaps are only visible. At this  $1^\circ$  resolution, used for comparison with~~  
 390 ~~the uniform/clear grid filter described in the previous paragraph, gaps are seen in regions~~

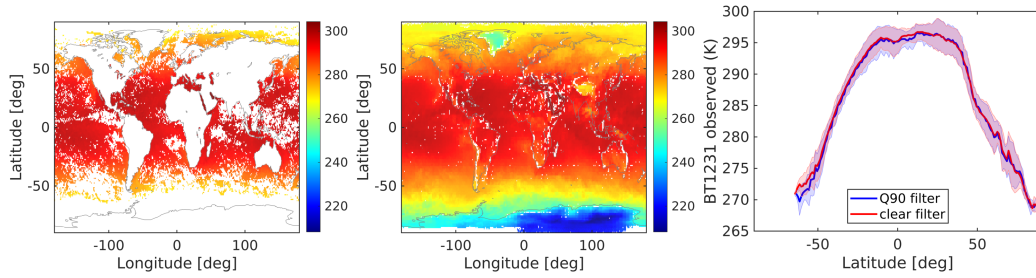


**Figure 2.** Clear scenes for the same 2012/08/27 - 2012/09/11 timespan selected by (left) an uniform/clear sky filter and (center) the Q0.90 integrated filter average described in this paper. The right hand plot shows the mean (over ocean) observed BT1231 as a function of latitude, for the two selections; the difference is about  $0 \text{ K} \pm 1 \text{ K}$  in most region except in the southern mid-latitudes where the integrated-Q0.90 filter average produced scenes that were about 1 K cooler on average.

391 where ~~there are for example mountains, or in the desert regions where other areas are even~~  
 392 ~~warmer. We note that increasing the quantile threshold to 0.95 or 0.97 did not introduce~~  
 393 ~~the gaps seen in the left hand (uniform/clear) map for example the local topography means~~  
 394 ~~observations over mountains would be colder than the surrounding coastal or plain regions.~~  
 395 ~~This is not a concern since zooming back out to the coarser  $3^\circ \times 5^\circ$  tile resolution, will~~  
 396 ~~include Q0.90 data for the quantile and trending analysis.~~

397 To compare the mean observations we ~~filter away remove~~ the over-land and over-  
 398 polar region data from the center plot. The right hand plot shows the mean observed  
 399 BT1231 from the  $1^\circ \times 1^\circ$  grid from the uniform/clear sky filter as a function of latitude,  
 400 compared to the  $1^\circ \times 1^\circ$  grid from the integrated-Q0.90 filter average. The difference between  
 401 the uniform/clear versus integrated-Q0.90 filter average is within about  $0.25 \text{ K} \pm 1 \text{ K}$   
 402 across the southern tropics to the northern midlatitudes, though the bias rises to about  
 403 1 K by about  $-50^\circ\text{S}$ . We consider this an acceptable difference, as we could tune the thresh-  
 404 olds for the uniform/clear filter to *e.g.* change the areal coverage and/or number of clear  
 405 scenes and hence comparisons to the Q0.90 scenes.

406

407 ~~We ran these tests for three~~ The results presented in this section have been checked  
 408 for robustness, using other 16 day intervals ~~in 2012,~~ spanning the four seasons. ~~The overall~~  
 409 ~~global bias and standard deviation for the 1231 channel between the co-located  $1^\circ \times 1^\circ$  grids~~  
 410 ~~by the uniform/clear filter and by the Q0.90 filter stayed fairly uniform, typically about~~  
 411  ~~$0.25 \text{ K} \pm 1 \text{ K}$ . From the information presented in this section, we~~ We conclude that for  
 412 any 16 day timestep the integrated-radiances used in the Q0.90 filter average (a) pro-  
 413 duces almost complete spatial coverage of the Earth, (b) selects scenes whose average  
 414 BT1231 is very close to the average BT1231 from scenes selected using a uniform/clear  
 415 filter (c) trends from that quantile typically differ by less than  $\pm 0.002 \text{ K} / \text{yr}^{-1}$  from  
 416 the other quantiles and (d) this selection produces spectral trends which compare well  
 417 against those obtained from the quality assured binned AIRS CCR data record Manning  
 418 (2022). Together these imply the integrated-Q0.90 average is an acceptable proxy for “clear  
 419 scenes”. For the remainder of the paper we ~~drop the word “integrated” and therefore~~ con-  
 420 sider Q0.90 as consisting of nominally clear observations whose BT1231 lies between the  
 421 90th quantile and hottest observation. Our retrievals using this Q0.90  $\rightarrow$  Q1.00 averaged  
 422 dataset (shortened to Q0.90) is referred to as AIRS\_RT in what follows.

### 3.2 Observed trends from the Q0.90 Quantiles

Having selected the Q0.90 observations, for each tile the average radiance per 16 day interval is computed. With two sixteen day periods not available (Aqua platform or AIRS shutdowns during *e.g.* solar flare events) this gives a total of 457 time steps over 20 years. Anomalies are formed from this time series, and then de-seasonalized to give the spectral radiance trends and error estimates Strow and DeSouza-Machado (2020) using Matlab *robustfit*:

$$r_{\text{observations}}^{16 \text{ days}}(t) \sim r_{\text{fit}}(t) = r_o + a_1 t + \sum_{i=1}^4 c_i \sin(n2\pi t + \phi_i) \quad (2)$$

with  $a_1$  and its associated uncertainty, both converted to brightness temperature (BT), being the trends in K  $\text{yr}^{-1}$ . Using sub-harmonics in the fit did not produce any noticeable change in the AIRS\_RT retrievals (described below).

The left panel of Figure 3 shows the descending orbit (nighttime) 20 year (September 2002- August 2022) global averaged spectral observations for the five quantiles mentioned above. We note the spectra in most of the plots in this section are weighted by the  $\cos(\text{latitude})$  of the tiles, unless otherwise stated. In addition we only show the 640-1640  $\text{cm}^{-1}$  region, and ignore the shortwave 2050-2750  $\text{cm}^{-1}$  region since the AIRS SW channels are drifting relative to the LW Strow and DeSouza-Machado (2020). Spectral averages constructed from Figure 1 would have this same behavior, namely that in the window region the mean spectrum of data populating the warmer quantiles integrated out to Q1.00 (Q0.80, Q0.90, Q0.95, Q0.97) as defined in Equation 1 are on the order of a Kelvin apart, and have about half/quarter that difference in the optically thicker regions dominated by  $\text{H}_2\text{O}$  and/or  $\text{CO}_2$  absorption respectively.

The right hand panel of Figure 3 shows (top) the trends and (bottom) the  $2\sigma$  trend uncertainties for these quantiles, in Kelvin/year  $\text{K yr}^{-1}$ . We emphasize that the top right panel shows that the spectral trends for the quantiles lie almost on top of each other; the difference between the Q0.50 and other trends is at most about  $+0.003 \text{ K yr}^{-1}$  (out of a  $0.02 \text{ K yr}^{-1}$  signal) in the window region (and about  $+0.0045 \text{ K yr}^{-1}$  in the troposphere temperature sounding channels), or less than 10%. Similarly the largest trend uncertainty in the bottom panel is for Q0.50. This implies that clouds effects in the infrared do produce the largest variability (blue curve) but on average for the infrared are not changing much, so the  $+0.022 \text{ K yr}^{-1}$  window region trends are dominated by surface temperatures changes and to a lesser extent by water vapor changes.

The TOA radiances in the 15 um (700-800  $\text{cm}^{-1}$ ) region is dominated by the are impacted by two effects (a) the increased optical depths due to increasing atmospheric  $\text{CO}_2$  increases; the effects of increasing are to make the atmosphere emit at leads to atmospheric emission from higher altitudes/lower temperatures, leading to an almost resulting in almost a  $-0.06 \text{ K/year}$  signal for the troposphere; hidden in there are the, and (b) the atmospheric temperature increases (again about  $+0.02 \text{ K yr}^{-1}$ ); also  $\text{yr}^{-1}$ ). Also of interest is the trends in the stratosphere (650-700  $\text{cm}^{-1}$ ) changes which consists of a stratospheric cooling signal (negative) and emission higher up due to increased  $\text{CO}_2$ ; combining to give a net zero effect over 20 years, also seen in Raghuraman et al. (2023). The  $\text{H}_2\text{O}$  signal is evident in the 1400-1625  $\text{cm}^{-1}$  region, and is negative; in other words, increasing temperatures have led to increased atmospheric amounts of  $\text{H}_2\text{O}$ , and the water vapor feedback has reduced the amount of outgoing flux in that region. By extension, this also happens in the Far Infrared regions affected by water vapor; current sounders do not make direct measurement in the 10-600  $\text{cm}^{-1}$  region so at present this can only be inferred; however in the near future it is anticipated the Far Infrared Outgoing Radiation Understanding and Monitoring (FORUM) mission Palchetti et al. (2020) will provide data to fill in this important gap in the future.

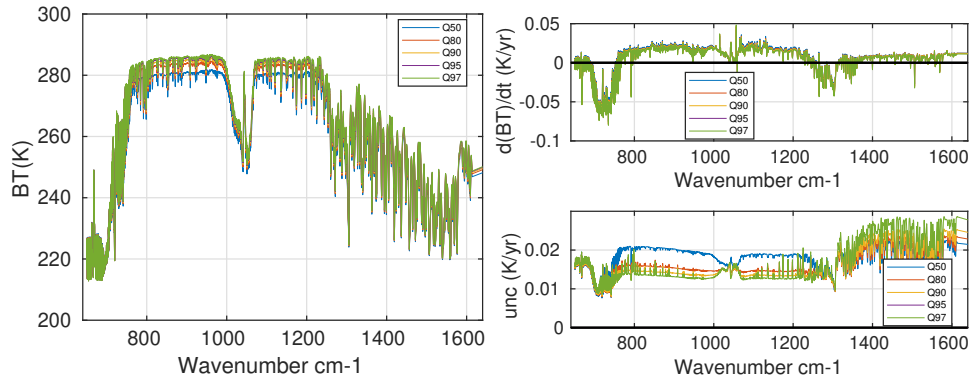


**Figure 3.** 20 year trends from different observation quantiles. The left hand panel shows the mean globally averaged BT trends-observations from 20 years of AIRS data, for quantiles 50,80,90,95,97 as described in the text. The right hand panel shows (top) the globally averaged trends from for those years-different quantiles and (bottom) the spectral uncertainty in the trends. The nighttime (descending) trends are shown in these plots.

471

472

### 3.3 Observed trend changes over 20 years

473

474

475

476

477

478

479

480

481

The left panel of Figure ?? shows the mean descending (nighttime) orbit Q0.90 brightness temperature spectrum, for four time periods, all commencing on September 1, 2002 – the periods are for 5,10,15,20 years of data and end on August 31, 2007, 2012, 2017, 2022 respectively. As expected the mean cosine averaged observed BT is slightly over 284 K through most of the longwave window region. The right hand panel of the same Figure ?? shows the trends for the four time periods in the top, while the bottom shows the uncertainties. Averaging over the inter-annual variability affects the trends, with the shortest/longest time periods (5/20 years) having the largest/smallest spectral uncertainty as one would expect as inter-annual variability slowly becomes less important in the trends.

482

483

484

485

486

Changes in AIRS observations over time spans of 05,10,15,20 years all beginning on September 1, 2002. The left hand panel shows the mean globally averaged 90th quantile BT spectra for those time periods. The right hand panel shows (top) the trends from those years and (bottom) the spectral uncertainty in the trends. The nighttime (descending) trends are shown in these plots.

487

488

## 4 Spectral closure : comparisons between observed and simulated spectral trends

489

490

491

492

493

494

495

496

497

498

499

Previous work Strow and DeSouza-Machado (2020) has demonstrated that the radiances from AIRS are climate quality, if one restricts the channel set to the  $\sim 450$  channel set that is largely immune to nonphysical drifts Strow et al. (2021). In this section we describe a way to test the quality of the monthly thermodynamic output from reanalysis and/or L3 products which are all in geophysical space, against the AIRS L1C observational data which is in radiance space. This is accomplished by geolocating the monthly (ERA5) surface temperature, air temperature, water vapor and ozone fields to tile centers as described in Section 2.2, which are then input and run through the SARTA fast model Strow, Hannon, DeSouza-Machado, et al. (2003), for the entire 20 years. Spectral radiance trends were then computed from these time series of (clear sky) spectral radiances. The conversion of L3 retrieval and NWP reanalysis trends to a radiance time

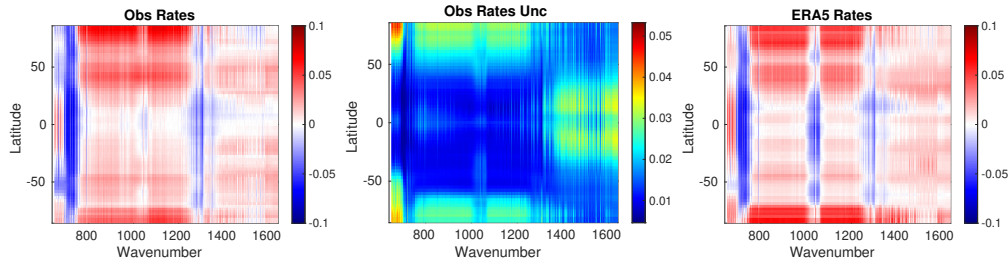


**Figure 4.** 20 year zonally averaged spectral brightness temperature trends (in  $\text{K /year}$ ) for (left) AIRS Q0.90 observations and (right) clear sky simulations using ERA5 monthly model fields. The center panel shows the AIRS Q0.90 spectral uncertainties. The ERA5 simulations included linear trends of  $\text{CO}_2$ ,  $\text{CH}_4$  and  $\text{N}_2\text{O}$ , while the  $\text{O}_3$  trends in ERA5 are from the reanalysis itself.

series, provides a rigorous check of their accuracy against the observed AIRS L1C radiance trends which are validated to be highly accurate.

~~A good reviewer might ask about the noise introduced by secant angle varying in the 16 day period. Check v~~

The simulations included realistic column linearly-increasing-with time mixing ratios for  $\text{CO}_2$ ,  $\text{CH}_4$  and  $\text{N}_2\text{O}$  for the ERA5 spectra, as well as land or ocean surface emissivity co-located to tile centers together with view angles of about  $22^\circ$ . From these the ERA5 spectral trends were derived similarly to what was described above for the AIRS observation spectral trends.

Figure 4 shows the descending (night) zonally averaged results in  $\text{K /year}$ , allowing us to compare the Q0.90 nominally clear AIRS observed spectral trends, to those simulated using monthly ERA5 fields (without clouds). The center panel shows the spectral trend uncertainties from the observations, also in  $\text{K /year}$ . In the next section we derive geophysical trends from these (AIRS observed) spectral trends, and the similarities/ differences in geophysical trends can be partially understood from the similarities/differences in the spectral trends. For example, the  $\text{H}_2\text{O}$  sounding region ( $1350\text{-}1600\text{ cm}^{-1}$ ) shows roughly similar (positive) trends in the tropics and mid-latitudes; there are some slight differences in the high altitude channels ( $1450\text{-}1550\text{ cm}^{-1}$  region). The following sections shows that there are subtle differences in these trends, which manifest as differences in tropospheric water vapor trends. Observations and simulations both have positive  $\text{dBT}/\text{dt}$  in the  $800\text{-}960, 1150\text{-}1250\text{ cm}^{-1}$  region, indicating surface warming; however the ERA5 simulation show more warming in the southern polar regions than do the AIRS observations. In particular note the mean warming in the tropics is less than that in the mid-latitudes, and the polar regions show the largest overall change in brightness temperature in the window region. Large differences are seen in the  $10\text{ }\mu\text{m}$  ( $1000\text{ cm}^{-1}$ )  $\text{O}_3$  sounding region, which are not surprising since ozone assimilation is not a primary goal of ECMWF assimilation; here we do not address these as we focus on the changes to the moist thermodynamic state. The window region trends computed using the ERA5 model are more positive in the Southern Polar region. Conversely the  $640\text{-}700\text{ cm}^{-1}$  spectral region is positive, especially in the tropics; however the observations show a net cooling trend away from the tropics, compared to the ERA simulations. This demonstrates the importance of the model  $\rightarrow$  spectral trend comparisons, given the accuracy of the AIRS observations.

534 The paper by (Raghuraman et al., 2023) shows similar figures, but in terms of spec-  
 535 tral OLR trends encompassing the 0-2000  $\text{cm}^{-1}$  range, while (Huang et al., 2023) shows  
 536 similar plots for a slightly smaller time period (2002-2020) and using nadir L1B radiance  
 537 dataset which has no or minimal frequency corrections compared to the L1C set we use  
 538 in this paper. (Huang et al., 2023; Raghuraman et al., 2023) and our work all show, ei-  
 539 ther in radiance or OLR space, (a) the increased observed radiance in the window chan-  
 540 nels, due to surface temperature increases (b) the  $\simeq -0.06 \text{ K } \cancel{\text{yr}^{-1}} \text{yr}^{-1}$  decrease in BT in  
 541 the 700-750  $\text{cm}^{-1}$  troposphere sounding region, which is due to the  $\text{CO}_2$  amounts increas-  
 542 ing; we also see differences in the signs of the BT changes in the 650-700  $\text{cm}^{-1}$  strato-  
 543 spheric  $\text{CO}_2$  and temperature channels for some latitudes between AIRS\_RT observa-  
 544 tions and ERA5 simulations (c) increases in the 1350-1640  $\text{cm}^{-1}$  water vapor sounding  
 545 region seen in Figures 3 and 5, and (d) the 1280-1340  $\text{cm}^{-1}$  decreases are due to  $\text{CH}_4$   
 546 increases.

#### 547 4.1 Sample spectral closure comparisons using other monthly products

548 Here we follow the earlier work of Huang et al. (2023) and convert the ERA5 monthly  
 549 model fields to spectral radiances, after which we compute spectral trends for compar-  
 550 ison to AIRS observations. Spectral closure calculations for the entire 20 year timeseries  
 551 were also generated for the monthly MERRA2 model fields, as well as the monthly AIRS  
 552 v7 L3 and CLIMCAPS L3 retrieved data products. Again only the monthly thermody-  
 553 namics and surface temperature fields for all  $72 \times 64$  tiles were used in these SARTA runs,  
 554 with GHG changes added in for each timestep as described above. Spectral trends were  
 555 then computed using Equation 2.

556 We chose just one limited example here to illustrate the power of this approach for  
 557 diagnosing which dataset is more accurate, given that the AIRS spectral trend accuracy  
 558 is already established. Water vapor is highly variable in space and time, meaning wa-  
 559 ter vapor retrievals using hyperspectral sounders radiances differ most from NWP fore-  
 560 casts, in particular because of the typical  $\pm 90$  minute difference between observation  
 561 and forecast, and is where these sounders typically provide the most information. Fig-  
 562 ure 5 show the globally averaged brightness temperature trends (in  $\text{K } \cancel{\text{year}^{-1}} \text{yr}^{-1}$ ) in the  
 563 1350 - 1650  $\text{cm}^{-1}$  water vapor sounding region. The blue curve shows the trends from  
 564 the AIRS observations used in this paper, while spectral trends constructed from the AIRS  
 565 L3/ CLIMCAPS L3 retrievals are in red/yellow and the ERA5 model fields are in pur-  
 566 ple. The AIRS observations and ERA5 constructed spectral trends are positive in this  
 567 region, while the AIRS L3 and CLIMCAPS L3 trends are obviously different, being neg-  
 568 ative in this water vapor sounding region. The subtle differences in these spectral trends  
 569 arise from differences in the geophysical trends between observations and the models them-  
 570 selves, and will be addressed in the following sections, where the retrieved and model sur-  
 571 face temperature, and atmospheric temperature and water vapor geophysical trends will  
 572 be compared and discussed.

## 573 5 Testing the variability of representative points from NWP modelsreanalysis

574 Each sixteen day  $3^\circ \times 5^\circ$  tile contains  $\sim 12000$  observations, which means for each  
 575 tile about 600 daytime and 600 nighttime observations are averaged to produce the Q0.90  
 576 dataset per timestep. Conversely there are typically only  $\sim 240$  monthly ERA5  $0.25^\circ$  points  
 577 per  $3^\circ \times 5^\circ$  tile; for  $1^\circ$  resolution AIRS L3 and CLIMCAPS L3 there are even fewer (15)  
 578 points per tile. This low number of points means we chose a simple solution of using the  
 579 grid cell closest to the center of each  $3^\circ \times 5^\circ$  tile for building the NWP and L3 geophys-  
 580 ical time series. This choice is validated below using the following test to see for exam-  
 581

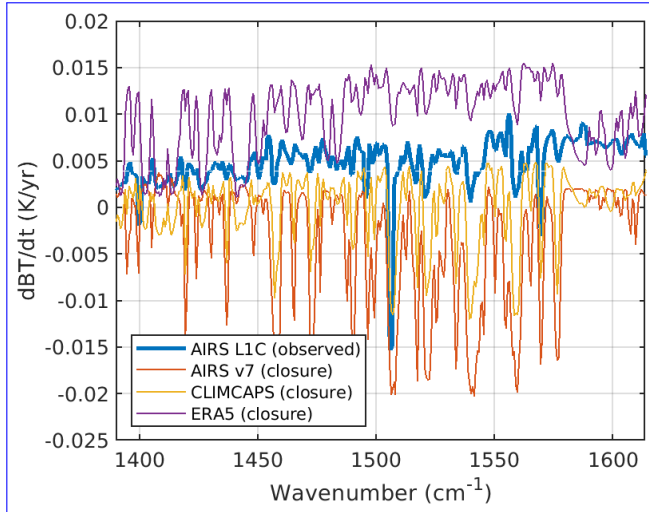


**Figure 5.** Globally averaged spectral trends in the water vapor sounding region : AIRS L1C observations (blue) compared to spectral closure from the standard monthly AIRS L3 retrievals (red) and CLIMCAPS L3 (yellow) and from monthly ERA5 simulations (yellow). The reconstructed AIRS\_RT trends very closely match the AIRS L1C observations and are not shown here.

582 ple how surface temperature trends would be impacted as we changed the representa-  
583 tive point for the ERA5 model fields.

584 For the descending overpass we built complete sets of approximately 240 ERA5 points  
585 per tile per month; at 0.25° resolution one of these is almost certainly at the tile center.  
586 From these monthly sets, we could either directly read the tile center temperature (our  
587 default), or compute the average surface temperature per tile, or compute the average  
588 of the hottest 10% surface temperatures per tile. This was done for all 20 years (240 monthly  
589 timesteps) after which the three timeseries were trended. Over ocean the differences be-  
590 tween all three datasets as was typically  $-0.001 \pm 0.005 \text{ K /year yr}^{-1}$ , while over land the  
591 differences were larger at about  $0.001 \pm 0.01 \text{ K /year yr}^{-1}$ . This is to be compared to  
592 mean trends of about  $0.014 \pm 0.02 \text{ K /yr yr}^{-1}$  over ocean and  $0.025 \pm 0.04 \text{ K /y over}$   
593 land. In other words  $\text{yr}^{-1}$  over land : the spread of the ocean and land ERA5 surface  
594 temperature trends for the three methods, was about four times larger than the spread  
595 of the differences between the three methods. In what follows is much smaller than the  
596 mean trends. Given that there were far fewer re-analysis points in a grid box than tiled  
597 Q0.90 observations, coupled with the fact that choosing the 10% warmest profiles would  
598 provide an even smaller sample, we chose to use the tile center was thus chosen as to be  
599 the representative point to co-locate the model fields, when comparing against the tiled  
600 observations.

## 601 6 Geophysical Trend Retrieval outline

### 602 6.1 Setting up the Retrieval Problem

603 The observed spectral brightness temperature for a tile at any time  $t$  can be mod-  
604 eled as

$$BT(\nu, t) = f(X(t), \epsilon(\nu, t), \theta(t)) + \text{NeDT}(\nu) \quad (3)$$

605 where the state vector  $X(t)$  has the following five geophysical state parameters : (1) sur-  
606 face temperature (ST), (2) atmospheric temperature profile  $T(z)$ , (3) water vapor pro-

file WV(z), (4) ozone profile O3(z) (5) greenhouse gas forcings (GHG) due to CO<sub>2</sub>, CH<sub>4</sub> and N<sub>2</sub>O changing as a function of time  $t$  and  $f(X(t), \epsilon, \theta, \nu)$  is the clear sky radiative transfer equation for channel center frequency  $\nu$ . The spectral noise  $NeDT(\nu)$  for a typical tropical “clear scene” is about 0.1 K in window region, increasing to about 1 K in the 15  $\mu\text{m}$  temperature sounding channels and about 0.2 K in the 6.7  $\mu\text{m}$  water vapor sounding region, but the noise will vary as a function of scene temperature. We ~~parameterize~~ parameterize the GHGs using single numbers (such as ppm(t) for the CO<sub>2</sub> column), and include the AIRS orbit and viewing angle geometry  $\theta$  and the surface emissivity  $\epsilon(\nu)$ , while we omit forward model and spectroscopy errors. We ignore cloud scattering as well as the spatial variation of the state parameters, emissivity and scan angle geometry within a tile. Linearizing the above equation about the time averaged profile, the relationship between the observed spectral trends and desired thermodynamic trends is given by

$$\frac{d\overline{BT}(\nu)}{dt} = \frac{\partial f}{\partial X} \frac{d}{dt} \overline{X(t)} = K(\nu) \frac{d}{dt} \overline{X(t)} + \cancel{K_{\text{emissivity}}(\nu) \frac{d}{dt} \epsilon(t)} \xrightarrow{0} K(\nu) \frac{d}{dt} \overline{X(t)} \quad (4)$$

where the matrix  $K(\nu)$  is the thermodynamic jacobian (surface temperature, air temperature and trace gases) and we ignore any orbit drifts (changes to  $\theta$ ), instrument changes (changes to  $NeDT(\nu)$ ) and surface emissivity ( $\epsilon(\nu)$ ); the last assumption is investigated in a later section. The overbars on parameters  $X$  denotes this is a time average (linear trend) that we are working with, and we have converted from radiances in Equation 2 to brightness temperatures in Equations 3 and 4.

## 6.2 Jacobian calculations

For a typical clear sky tropical sky atmosphere, the 800 - 1200  $\text{cm}^{-1}$  window region has surface temperature (SKT) jacobians which are about +0.5 to +0.75 K per degree SKT change and -0.75 to -0.25 K per 10% change in column water vapor. The spectral variability in these window region jacobians is primarily due to reducing water continuum absorption as you move from the 800  $\text{cm}^{-1}$  end to the 1200  $\text{cm}^{-1}$ ; consequently the surface temperature jacobians becomes closer to unity and the column water jacobians become closer to zero as water vapor amount decreases (drier atmospheres in the mid-latitudes and polar regions). The hyperspectral channels used in this work help separate out these two competing changes, which we validate against other datasets in this study. As seen in Figure 4 typical magnitudes of the spectral trends on the left hand side of Equation 4 are less than about 0.1 K per year. Equation 4 is in the usual inversion form  $\delta y = K\delta x$ , and the Optimal Estimation (Rodgers, 2000) solution used to solve the anomaly time series in Strow et al. (2021) is also used here. The noise term used for the trend retrieval  $NeDT(\nu)$  is not the instrument noise since each 16 day point in our time series is averaged over hundreds of observations as earlier described; instead the uncertainty is that due to inter-annual variability in the linear trends obtained from the trend fitting in Equation 2. Examples of typical noise values are shown in the bottom right hand ~~panels~~ panel of Figures 3 ~~and ??~~.

ERA5 monthly model fields at tile centers, together with time varying concentrations of GHG such as CO<sub>2</sub>, were averaged over 20 years so jacobians could be computed. The GHG concentrations were a latitude dependent increase of about  $\sim 2.2$  ~~ppmv/year~~ ppm yr<sup>-1</sup> for CO<sub>2</sub> derived from the CarbonTracker Peters et al. (2007) (CarbonTracker CT-NRT.v2023-4, <http://carbontracker.noaa.gov>) model data at 500 mb. Our pseudo-monochromatic line by line code kCARTA De Souza-Machado et al. (2018, 2020) was used with these averaged profiles to produce accurate analytic jacobians. The HITRAN 2020 line parameter database Gordon and Rothman (2022), together with MT-CKD 3.2 and CO<sub>2</sub>,CH<sub>4</sub> line mixing from the LBLRTM suite of models Clough et al. (2005) were used in the kCARTA optical depth database De Souza-Machado et al. (2018). A 12 month geographical land-varying spectral emissivity database spanning one year from Zhou et al. (2011) was used, while ocean emissivity came from Masuda et al. (1988). The atmospheric



656 temperature, water vapor and ozone profile jacobians, and the surface temperature and  
 657 column jacobians for the GHG gases such as CO<sub>2</sub> and CH<sub>4</sub> and N<sub>2</sub>O, were then convolved  
 658 using the best estimate AIRS Spectral Response Functions Strow, Hannon, Weiler, et  
 659 al. (2003).

660 Tests done for this paper, together with the results in Strow et al. (2021), estab-  
 661 lished that jacobians derived from MERRA2 versus ERA5 produced no significant dif-  
 662 ferences in the context of retrieved trends or anomalies done for this paper, as the un-  
 663 certainty in linear trends due to inter-annual variability dominates over any uncertainty  
 664 (or differences between) model fields.

### 665 **6.3 Optimal Estimation Retrieval : State vector, covariance matrices** 666 **and *a-priori***

667 Using monthly ERA5 model fields averaged over 20 years, for each of the  $64 \times 72$   
 668 tiles we computed analytic jacobians for the following (vector) atmospheric thermody-  
 669 namic variables [fractional water vapor, fractional ozone and temperature] together with  
 670 (scalar) surface temperature, where we retrieved fractional gas concentration trends  $dfrac{X}/dt =$   
 671  $1/X_{avg}(z)dX_{avg}(z)/dt$  to keep all values in the state vector at about the same magni-  
 672 tude. A single iteration Optimal Estimation retrieval Rodgers (2000) is used to simul-  
 673 taneously solve for the geophysical parameter trends. As in (Strow & DeSouza-Machado,  
 674 2020) the geophysical covariance uncertainty matrices are a combination of Tikonov and  
 675 covariance regularization. The uncertainties for the covariance matrices were typically  
 676  $[0.1, 0.25, 0.45]$  K ~~/yr~~yr<sup>-1</sup> for the surface/tropospheric/stratospheric temperature trends,  
 677 and  $[0.04/0.02]$  ~~/year~~yr<sup>-1</sup> for the fractional tropospheric/stratospheric water vapor trends.  
 678 Tikonov L1 regularization (Rodgers, 2000) also included, with the scalar factor multi-  
 679 plying this regularization corresponding to about 1/10 the covariance uncertainties. The  
 680 spectral uncertainties used in the retrievals come from the above mentioned trend un-  
 681 certainties. For completeness we note that a sequential retrieval (see for example Smith  
 682 and Barnett (2020)) produces very similar geophysical trends.

683 Here we emphasize four points about our geophysical trend retrievals, which sets  
 684 us apart from trends derived from other datasets. Firstly the *a-priori* trend state vec-  
 685 tor is zero ( $dST/dt = dT(z)/dt = dQ(z)/dt = 0$ ) for all geophysical parameters, except  
 686 for water vapor where we enforced constant (or slightly increasing) relative humidity as  
 687 described below. This ensures traceability of our retrieval is straightforward especially  
 688 wherever the AIRS instrument has sensitivity. For example the 300 - 800 mb water va-  
 689 por trend retrievals will be based on the data only, thereby insulating us from any pos-  
 690 sible *a-priori* information from *e.g.* climatology or NWP models, unlike the operational  
 691 AIRS V7 or CLIMCAPS retrievals which use first guesses based on neural net and MERRA2  
 692 respectively.

693 Secondly as seen in Figures 4 and 5, in the 15  $\mu m$  region there is a large spectral  
 694 overlap signal ( $-0.06$  K ~~/yr~~yr<sup>-1</sup>) from the increasing CO<sub>2</sub>, which is much larger than the  
 695 expected atmospheric temperature trend ( $0.01$  K ~~/yr~~yr<sup>-1</sup>). ~~The 20-year dataset contains inter-annual~~  
 696 ~~variability whose noisy time series and correlations with for example temperature changes,~~  
 697 ~~which yr<sup>-1</sup>. These correlations~~ makes it difficult to ~~also retrieve these well-mixed GHG.~~  
 698 ~~Instead of attempting to solve for both GHG concentration changes and for temperature~~  
 699 ~~changes, we spectrally removed jointly retrieve both temperatures changes and changes~~  
 700 ~~in well mixed GHGs such as CO<sub>2</sub>. We chose to focus on retrieving temperature changes~~  
 701 ~~only, by spectrally removing~~ the effects of changing ~~ed~~CO<sub>2</sub>, CH<sub>4</sub> and N<sub>2</sub>O GHG con-  
 702 centrations, ~~. This was done~~ by using the GHG trends estimated from NOAA ESRL Car-  
 703 bonTracker data multiplied by the appropriate GHG gas column jacobian (CO<sub>2</sub>, N<sub>2</sub>O and  
 704 CH<sub>4</sub> and CFC11, CFC12) computed as described above using the averaged over 20 years  
 705 ERA5 monthly profile for each tile.

706 Thirdly instead of using all 100 layers described in the AIRS forward model Strow,  
 707 Hannon, DeSouza-Machado, et al. (2003), we combine pairs of layers for a 50 atmospheric  
 708 layer retrieval, as the AIRS radiances contain far fewer than 100 pieces of information  
 709 (see *e.g.* Maddy and Barnet (2008); De Souza-Machado et al. (2018)).

710 Fourthly, modern hyperspectral infrared sounders have highest sensitivity to tem-  
 711 perature and water vapor in the mid-tropopause; see for example the averaging kernels  
 712 in Irion et al. (2018). Using a zero fractional WV trends *a-priori* at all levels, it was fairly  
 713 straightforward to obtain fractional WV(z) trends close to those from the NWP model  
 714 datasets in the ~~3000-850~~ 300-850 mb region. In order to improve our results in the low-  
 715 est layers, we enforced a constant relative humidity approximation, which is a well-known,  
 716 expected behavior under global climate change Soden and Held (2006); Sherwood et al.  
 717 (2010). This was done by ~~using the~~ ignoring the contribution due to water vapor changes  
 718 in the observed BT1231 trend, and using it as an approximation for air temperature trend  
 719 over ocean; this allows us to compute an estimate of how the water vapor would need  
 720 to change

$$RH(T) = \frac{e}{e_{sat}(T)} \implies \delta(RH) = \frac{1}{e_{sat}(T)} \delta e - \frac{e}{e_{sat}^2(T)} \delta e_{sat}(T) = \frac{1}{e_{sat}(T)} \delta e - \frac{e}{e_{sat}(T)} \frac{L_v}{R_v} \frac{1}{T^2} \delta T \quad (5)$$

721 where  $e, e_{sat}(T)$  are the vapor pressures and we used  $e_{sat}(T) = e_{s0} e^{\frac{L_v}{R_v} (\frac{1}{T_0} - \frac{1}{T})}$  (where  
 722  $L_v, R_v$  are latent heat of vaporization and gas constant respectively) to go from the ex-  
 723 pression in the center to the expression on the right. If we expect the change in RH to  
 724 be zero then  $\frac{\delta e}{e} = \frac{L_v}{R_v} \frac{\delta T}{T^2}$ , where we can use  $\delta T / \delta t \sim d/dt BT1231$ . to approximate the  
 725 *a-priori* fractional vapor pressure rates (or *a-priori* fractional water vapor rates) between  
 726 surface and 850 mb, smoothly tailing to 0 in the upper atmosphere. Subsection 7.2 has  
 727 a similar discussion on a proposed method to alleviate the lack of sensitivity to upper  
 728 atmosphere water vapor. Our default results in this paper are from using the MLS *a-*  
 729 *priori*, unless otherwise stated.

#### 730 6.4 Testing on ~~Synthetic Spectra~~ synthetic trend spectra made from ERA5 731 Reanalysis monthly fields

732 We tested the retrieval code by using it on the simulated nighttime only ERA5 spec-  
 733 tral trends, and compared to geophysical trends computed directly from the ERA5 re-  
 734 analysis model. Spot checks of the spatial correlations of ERA5 fractional water vapor  
 735 and temperature trends versus the trends retrieved from synthetic spectra/our retrieval  
 736 algorithm, peaked at 500 mb with correlations of about 0.9, compared to 800 mb cor-  
 737 relations of 0.80 and 0.55 for temperature and fractional water vapor trends respectively  
 738 and 200 mb correlations of 0.89 and 0.69 for  $dT/dt, dWVfrac/dt$ . This is to be expected  
 739 since a computation of the water vapor averaging kernels for infrared instruments for ar-  
 740 bitrary atmospheric profiles typically shows they peak in the 300 mb - 850 mb range and  
 741 decrease rapidly away from those regions; conversely the temperature averaging kernels  
 742 stay relatively uniform through the free troposphere and above, though they also decrease  
 743 close to the surface; see for example Irion et al. (2018); Smith and Barnet (2020); Wu  
 744 et al. (2023).

745 Figure 6 shows a sample set of results using nighttime ERA5 model output converted  
 746 to spectral trends as described above. The top panels (A) are always the atmospheric  
 747 trends ~~derived direct~~ computed directly from the monthly ERA5 model fields, while the  
 748 bottom panels (B) are the atmospheric trends ~~derived retrieved~~ from the converted ERA5  
 749 spectral brightness temperature trends. The left most panel is the atmospheric temper-  
 750 ature trend comparison (both in  $K$  ~~/yr~~  $yr^{-1}$ ) while the rightmost panel is the fractional  
 751 atmospheric water vapor trend comparison (in ~~/yr~~  $yr^{-1}$ ).

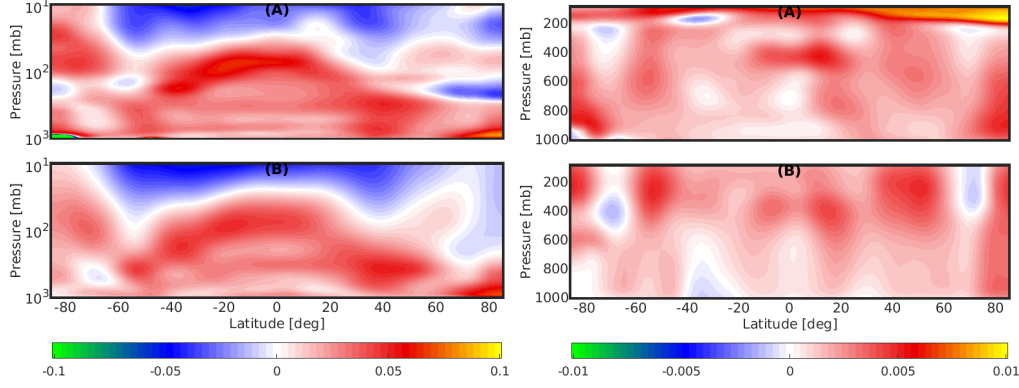


**Figure 6.** Comparing geophysical trends derived directly from ERA5 monthly nighttime fields (top) vs from the OEM retrieval applied to the spectral trends (bottom). Left panel is  $dT/dt$  (in  $K /year/yr^{-1}$ ) while rightmost panel is  $d(\text{fracWV})/dt$  (colorbar in  $/yr^{-1}$ ).

753 It is evident from the figure that the tropospheric trends in the tropical and mid-  
 754 latitude regions are quite similar, and there are differences in the polar regions and strato-  
 755 spheric regions where the AIRS instrument has reduced sensitivity. The atmospheric and  
 756 surface trends are shown in Table 1, divided into “all” (which is the entire  $\pm 90$  latitude  
 757 range and 0-1000 mb vertical range) and “T/M” which is the tropical/midlatitude region,  
 758 which is further reduced to 050-900 mb for air temperature and 300-800 mb for water  
 759 vapor. “ERA5 direct” are trends computed directly from the geophysical fields, while “ERA5  
 760 spectral” are retrieved from the spectral trends.

	$dTz/dt$ K $/year/yr^{-1}$ A <u>GND-TOA-SFC-TOA</u>	$dTz/dt$ K $/year/yr^{-1}$ T/M 050-900 mb	$dSKT/dt$ K $/year/yr^{-1}$ A	$dSKT/dt$ K $/year/yr^{-1}$ T/M	$d\text{fracWV}/dt$ K $/year/yr^{-1}$ A GND-TOA	$d\text{fracWV}/dt$ K $/year/yr^{-1}$ T/M 300-800 m
<u>ERA5 direct</u>	$0.010 \pm 0.038$	$0.029 \pm 0.013$	$0.020 \pm 0.035$	$0.018 \pm 0.032$	$0.003 \pm 0.002$	$0.002 \pm 0.001$
<u>ERA5 spectral</u>	$0.004 \pm 0.033$	$0.027 \pm 0.012$	$0.019 \pm 0.033$	$0.016 \pm 0.029$	$0.001 \pm 0.001$	$0.002 \pm 0.001$

**Table 1.** Cosine weighted air temperature, skin temperature, fractional water vapor trends, together with uncertainties. The “ERA5 direct” are directly from the ERA5 geophysical trends, while “ERA5 spectral” are trends retrieved from the converted ERA5 spectral trends.

## 6.5 Surface emissivity changes

761 Equation 3 explicitly includes the surface emissivity in the equation of radiative  
 762 transfer; however Equation 4 assumes this is unchanging. Here we rewrite Equation 4  
 763 as  
 764

$$\frac{d\overline{BT}(\nu)}{dt} - K_{emissivity}(\nu) \frac{d\overline{\epsilon(t)}}{dt} \rightarrow \frac{d\overline{BT}'(\nu)}{dt} = K(\nu) \frac{d\overline{X(t)}}{dt} \quad (6)$$

765 First we consider ocean emissivity changes Ocean emissivity has a dependence on  
 766 windspeed Masuda et al. (1988). Lin and Oey (2020) and other literature suggest wind  
 767 speed increases of  $+2.5 \text{ cm /s/year-s}^{-1} \text{ yr}^{-1}$  have occurred between 1993-2015 in the tropical  
 768 Pacific, and smaller (or close to zero) values elsewhere. The monthly ERA5  $u_{10}, v_{10}$

769 10 m speeds for the 20 year time period in this paper also showed the maximum abso-  
 770 lute trend was 0.09 m/s/year (over the Southern Ocean) while the global ocean mean  
 771 and standard deviation were  $0.006 \pm 0.022$  m ~~/s/years~~<sup>-1</sup> ~~yr~~<sup>-1</sup>; The emissivity changes  
 772 over ocean using a  $0.025$  m ~~/ss~~<sup>-1</sup> wind speed change are on average on the order of  $1 \times$   
 773  $10^{-6}$  per year in the thermal infrared window (or about  $0.0003$  K ~~/yr~~<sup>-1</sup> ~~yr~~<sup>-1</sup> change in the  
 774 window region); assuming the optical properties of water do not substantially change with  
 775 the  $\sim 0.02$  K increases seen in all the datasets considered in this paper, these very small  
 776 emissivity changes are of no consequence.

777 Land emissivity changes were estimated as follows. A global monthly mean emis-  
 778 sivity database, the Combined ASTER and MODIS Emissivity over Land (CAMEL v003)  
 779 has recently been released Borbas et al. (2018). We matched the tile centers to the database  
 780 for the  $20 \times 12$  months spanning our 2002/09 - 2022/08 time period, and computed the  
 781 emissivity trends over land; the results (not shown here) were on the order of  $-1 \times 10^{-4}$   
 782 and  $+3 \times 10^{-4}$  in the 800-960  $\text{cm}^{-1}$  and 1100-1250  $\text{cm}^{-1}$  regions respectively, averaged  
 783 over the land observations. For each tile the  $K_{emissivity}(\nu) \frac{d}{dt} \epsilon(t)$  term was estimated by  
 784 running SARTA with the default emissivity, then differencing with the SARTA output  
 785 obtained when the emissivity trends were added on. Averaged over the planet, the spec-  
 786 tral changes arising from these emissivity changes were much smaller than the spectral  
 787 trends seen in Figure 3, about  $-0.001$  K ~~/year~~<sup>-1</sup> ~~yr~~<sup>-1</sup> between 800-960  $\text{cm}^{-1}$  and about  $+0.002$   
 788 K ~~/year~~<sup>-1</sup> ~~yr~~<sup>-1</sup> on the 1100-1250  $\text{cm}^{-1}$  region (which we do not use in our retrieval, since  
 789 many of the channels are synthetic and the real channels are drifting (Strow et al., 2021)).  
 790 The land only results were roughly ~~about~~ three times these magnitudes. Using these emis-  
 791 sivity jacobians on the left hand side of Equation 6 and running the retrieval on the ad-  
 792 justed spectral trends over land, resulted in about at most 0.01 K increases to the zon-  
 793 ally averaged surface temperature changes over land; zonally averaged these largest dif-  
 794 ferences were at about  $40^\circ\text{N}$  to  $60^\circ\text{N}$  and  $-25^\circ\text{S}$  to  $+15^\circ\text{N}$ , due to emissivity decreases;  
 795 the  $20^\circ\text{N}$  to  $+35^\circ\text{N}$  region which included the Sahara and swathes of Asia, had emissiv-  
 796 ity increases but the averaged-over-land temperature decreases were small, as there were  
 797 offsetting emissivity increases in other land areas at the same latitudes. We did not pur-  
 798 sue the impact of these emissivity changes further as the CAMEL database is affected  
 799 by the stability of the MODIS data, and our results below will not include accounting  
 800 for changes in land emissivity.

## 801 7 Results

802 The trends retrieved in the previous section using simulated radiance trends show  
 803 that the retrieval package is working as expected. Here we apply our retrieval to observed  
 804 AIRS L1C radiance trends and discuss the retrieved AIRS\_RT geophysical trends to those  
 805 computed directly from the ERA5/MERRA2 model fields and AIRS L3/CLIMCAPS L3  
 806 products. We will have an expectation that since the simulated radiance trends had no  
 807 noise added to them, the uncertainty in the spectral rates was lower than the actual ob-  
 808 served spectral uncertainty; this will lead to larger uncertainties and/or errors in our re-  
 809 trieval using observed radiance trends.

810 We will make most comparisons against NWP models and L3 products in the con-  
 811 text of averages over the descending/night (N) and ascending/day (D) data since the MERRA2  
 812 (and GISS) datasets are only available as a D/N average; the reader is referred to the  
 813 Appendix where we show a few of the D-N differences. The results are shown in the or-  
 814 der of surface/column trends (surface temperature and column water), followed by zonal  
 815 averages of the atmospheric temperature and fractional water vapor trends.

### 816 7.1 Skin Temperature trends

817 There are typically multiple (window) channels that are sensitive to a surface pres-  
 818 sure, meaning the radiances typically have more information content for the surface tem-

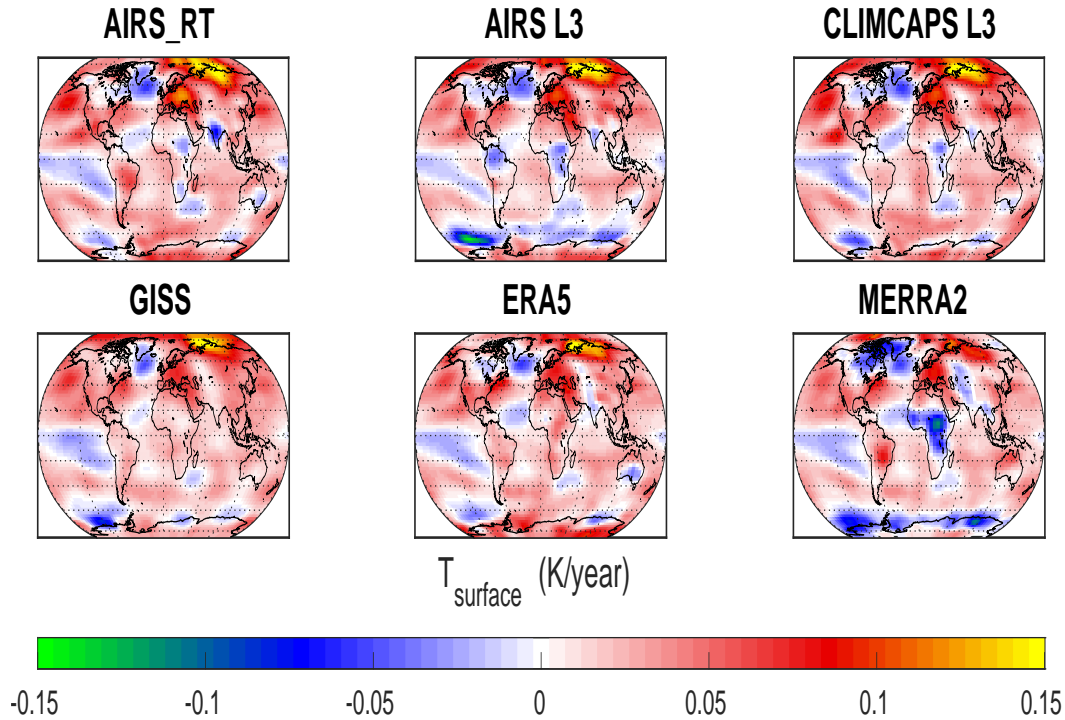


**Figure 7.** Surface temperature trends  $dSKT/dt$  averaged over day and night for AIRS\_RT, and from separately fitting the monthly data in ERA5, MERRA2, AIRS L3, CLIMCAPS L3 and GISS.

819 perature (assuming the surface emissivity is well known and there are no clouds) rather  
 820 than for example air temperature. Figure 7 shows the diurnally averaged day/night (D/N)  
 821 surface temperature trends from 6 datasets : AIRS\_RT, AIRS L3, CLIMCAPS L3, ERA5,  
 822 MERRA2 and NASA GISTEMP. AIRS\_RT shows an overall global warming of  $+0.021$   
 823  $\text{K } \overline{\text{year}}^{-1}$ ; the cooling trends include the tropical eastern Pacific and south of Green-  
 824 land and tropical northern Atlantic. The rest of the datasets also show similar patterns  
 825 of cooling in the N. Atlantic Ocean, warming over the Arctic and some degree of cool-  
 826 ing over the Antarctic Ice Shelf/Southern Ocean as does AIRS\_RT. The AIRS v7 L3  
 827 shows some cooling over Central Africa and the Amazon not seen in the AIRS\_RT trends,  
 828 where one could expect Deep Convective Clouds and possible cloud clearing issues. We  
 829 also point out the AIRS L3 product has many missing values off the western coasts of  
 830 N. and S. America, due to cloud clearing issues. MERRA2 shows more cooling over C.  
 831 Africa, and just like the AIRS v7 data, a lot of cooling near the Antarctic Ice Shelf. Of  
 832 note here is that although CLIMCAPS uses MERRA2 as its first guess, their surface tem-  
 833 perature trends are not similar, especially around the Antarctic where MERRA2 shows  
 834 strong cooling trends. Over the ocean GISS shows similar trends to what AIRS\_RT trends  
 835 show. An earlier study of Land Surface Temperatures between 2003-2017 using MODIS  
 836 Prakash and Norouzi (2020) shows very similar large daytime cooling trends over parts  
 837 of central and western Indian subcontinent that we see from our retrieval as well as di-  
 838 rectly from the BT1231 channel trends; for tiles that straddle both ocean and land the  
 839 quantile method picks up the hottest observations, which especially during summer are  
 840 mostly over the Indian subcontinent. For these reasons we also have confidence in our  
 841 retrieved cooling trends over for example daytime continental Central/Eastern Africa,  
 842 which are different from the other four day/night datasets.

843

844 The spatial correlations between AIRS\_RT retrieved rates and the various datasets  
 845 is shown in Table 2 while the cosine weighted skin temperature trends are shown in Ta-  
 846 ble 3. By adding in the uncertainty in the trends for any of the individual models or datasets,  
 847 and then doing the cosine weighting, we estimate uncertainties of about  $\pm 0.015 \text{ K } \cancel{\text{year}}\text{yr}^{-1}$   
 848 for “ALL”; the uncertainties for “OCEAN” are typically about 2/3 of that value, and for  
 849 “LAND” are about 4/3 of that value. We emphasize here that we use all available NWP  
 850 and L3 model data when computing their trends for any grid box, while the AIRS\_RT  
 851 uses only the hottest 10% of “clear” data; Strow and DeSouza-Machado (2020) showed  
 852 that the tropical retrieved surface temperature trends and anomalies over ocean corre-  
 853 lated very well with those from the ERA-I Sea Surface Temperature dataset.

ERA5	MERRA2	AIRSL3	CLIMCAPSL3	GISS
0.72	0.59	0.80	0.89	0.77

**Table 2.** Correlations of average (nighttime,daytime) retrieved skin temperature trends from AIRS\_RT, versus trends from models/products

SKT trend K $\cancel{\text{year}}\text{yr}^{-1}$	AIRS_RT	AIRS	CLIMCAPS	ERA5	MERRA2	GISS
ALL	0.020	0.017	0.021	0.023	0.011	0.021
TROPICS	0.011	0.011	0.012	0.016	0.010	0.015
MIDLATS	0.029	0.020	0.028	0.026	0.020	0.026
POLAR	0.032	0.028	0.033	0.041	-0.005	0.028
OCEAN	0.019	0.011	0.019	0.017	0.012	0.017
LAND	0.022	0.030	0.024	0.038	0.010	0.030

**Table 3.** Cosine weighted skin temperature trends; uncertainties are on the order of  $\pm 0.015 \text{ K}$  as explained in the text.

854 A notable outlier in this group is the MERRA2 trends, especially over land and  
 855 the Southern Ocean which are noticeable negative (blue) compared to the other datasets;  
 856 the agreement with tropical and mid-latitude oceans is much better. As noted earlier,  
 857 the MERRA2 monthly trends come from a combination day/night dataset that was down-  
 858 loaded, which as seen in Figure 7 consists of trends that are both positive and negative,  
 859 combining to get a closer-to-zero global weighted trend. In addition MERRA2 is the only  
 860 one of the six that (a) does not have the extreme  $+0.15 \text{ K } \cancel{\text{year}}\text{yr}^{-1}$  warming in the  
 861 northern polar region and (b) shows a lot of cooling in the Central African area. Using  
 862 ERA5 monthly data, we devised a test similar to the one mentioned in Section 5 to de-  
 863 termine if the differences between MERRA2 and ERA5 surface temperature trends could  
 864 be due to the temporal sampling (once for MERRA2 versus eight times for ERA5). For  
 865 each month we matched the eight ERA5 timesteps available per month to the tile cen-  
 866 ters and then averaged the surface temperatures per month; the ensuing geophysical time-  
 867 series was then trended. The day/night ERA5 average of Figure 7 was compared to these  
 868 trends; of note are (a) we did not see the cooling in Africa and near the Antarctic that  
 869 is seen in MERRA2 and (b) the main differences between the 1.30 am/1.30 pm average  
 870 in the bottom middle (ERA5) panel were over land (all 5 continents); the histograms of  
 871 the differences showed the peak was typically close to  $0 \text{ K } \cancel{\text{year}}\text{yr}^{-1}$ , but the widths over  
 872 land were about  $\pm 0.02 \text{ K } \cancel{\text{year}}\text{yr}^{-1}$  or less (compared to  $\pm 0.005 \text{ K } \cancel{\text{year}}\text{yr}^{-1}$  over ocean).

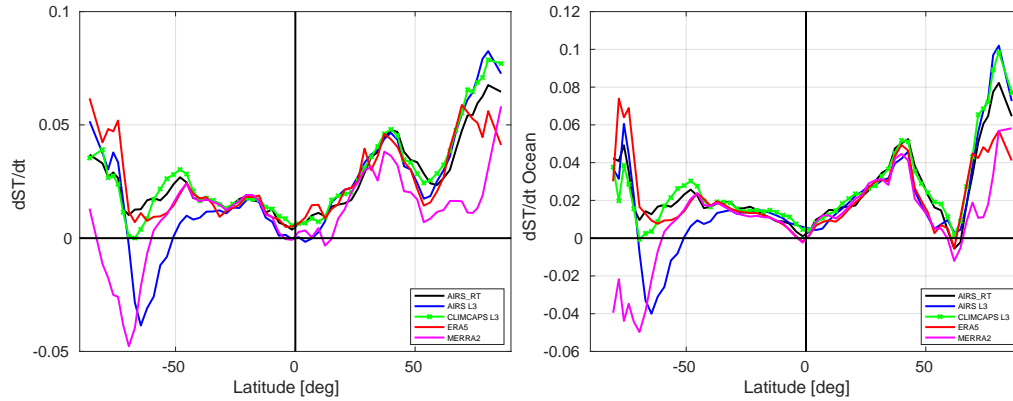


**Figure 8.** Zonally averaged surface temperature trends for (left) sum of ocean and land point and (right) ocean only.

873 Both AIRS L3 and MERRA2 show cooling in the Southern Ocean; we note that although  
 874 MERRA2 is the *a-priori* for CLIMCAPS L3, their trends are different than those from  
 875 MERRA2; in fact AIRS\_RT shows the closest correlation to the observational CLIM-  
 876 CAPS L3 trends. The AIRS L3 trends in the Southern Ocean region could arise because  
 877 of problems identifying ice during the L2 retrieval (private communication : Evan Man-  
 878 ning (JPL) and John Blaisdell (NASA GSFC)) though the MERRA2 trends also show  
 879 significant cooling in that region, where few surface observations from buoys poleward  
 880 of 60° exist to help resolve these differences (see for example Figure 10 in Haiden et al.  
 881 (2018)).

882 Figure 8 shows the zonally averaged total (land+ocean) and ocean only surface tem-  
 883 perature trends. Notice how the equator to midlatitude ocean trends are almost linear  
 884 for all datasets, with the slope for the northern hemisphere being about double that of  
 885 the southern hemisphere (roughly 0.001 K /year-yr<sup>-1</sup> per deg latitude). Again focusing  
 886 on the right hand plot, the AIRS L3 trends are negative in the Southern Ocean regions,  
 887 compared to the other 3 datasets, due to the cooling trends around the Antarctic continent  
 888 shown earlier, but then agrees with most of the other datasets over the Antarctic; the MERRA2  
 889 trends significantly differ between -90 S and -50 S. MERRA2 and ERA5 also show slightly  
 890 smaller warming trends in the Northern Polar, compared to the three AIRS-based datasets.  
 891

892

893 We point out that the trends seen in Figure 7 vary noticeably at more local, regional  
 894 levels and furthermore this spatial variation can differ between daytime and nighttime,  
 895 evident in Figure A1 of Appendix Appendix A, and that the observational sets (AIRS\_RT,  
 896 CLIMCAPS L3 and AIRS L3) had larger differences than ERA5. Discussing the possi-  
 897 ble causes of this is outside the scope of the paper.

## 898 7.2 Addition of Microwave Limb Sounder Water Vapor A-priori

899 The Microwave Limb Sounder (MLS), on board NASA's Aura platform, is designed  
 900 for sounding of the atmosphere above 300 mb. We computed water vapor trends from  
 901 the L3 data produced for that instrument (above 300 mb) and used them as an a-priori for  
 902 the AIRS\_RT retrieval.

903

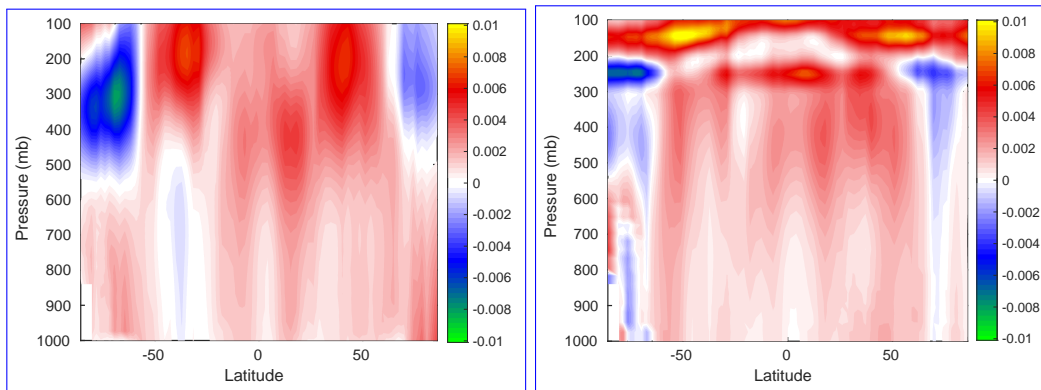


Figure 9.  $dWVfrac/dt$  (left) without and (right) with MLS *a-priori* in the upper atmosphere

Figure 9 shows the retrieved fractional water vapor trends when the *a-priori* trend in the upper atmosphere in the left and right panels were zero, or used MLS trends, respectively. One sees that the additional information brought in by the instrument sensitive to upper troposphere humidity, significantly changes the water vapor sounding especially in the polar region by moving towards the MERRA2 and ERA5 fractional water vapor trends seen in Figure 13. We note that the results shown in this paper use the MLS *a-priori*.

### 7.3 Column water vapor trends

Column water vapor trends provide an assessment of the water vapor retrieval quality in the lower atmosphere since this is dominated by the layers near the surface. For a hyperspectral infrared sounder over ocean the 1226 (Channel ID 1511) and 1231 (Channel ID 1620) spectral points are similarly impacted by surface emissivity and absorption by the water vapor information in the lowest layers is best retrieved using the weak water lines in thermal infrared region. This part of the retrieval is significantly complicated by the simultaneous presence of nonzero surface temperature, air temperature and water vapor jacobians in this spectral region, meaning the AIRS instrument has much reduced sensitivity to the water vapor continuum. However the 1226 channel is on the wing of a weak water vapor line and has additional absorption from the atmospheric water vapor column. Subtracting the observed brightness temperatures of these two channels  $BT_{1231} - BT_{1226}$  is therefore a representative approximation to (but is not equal to) the column water, just as  $BT_{1231}$  is a representative approximation to (but is not equal to) surface temperature. For example, using the simulated AIRS L1C clearsky radiance dataset over ocean we constructed for this paper using ERA5 monthly fields, we can regress the ERA5 column water against the brightness temperature difference to obtain  $mmw \sim 5.6 (BT_{1231} - BT_{1226}) + 1.0$ ; over land the emissivity could vary rapidly enough that this approximation breaks down vapor amounts in these lowest layers. In addition the changing concentration of very minor gases such as CFC-11 and CFC-12 Strow and DeSouza-Machado (2020) are quite evident in the spectral trends, further complicating the water vapor trend retrieval for the lowest layers.

The left hand panel of

Figure 10 shows the zonally averaged column water vapor trends, while the right hand panel shows the zonally averaged  $BT_{1231} - BT_{1226}$  trend (notice the multiplication



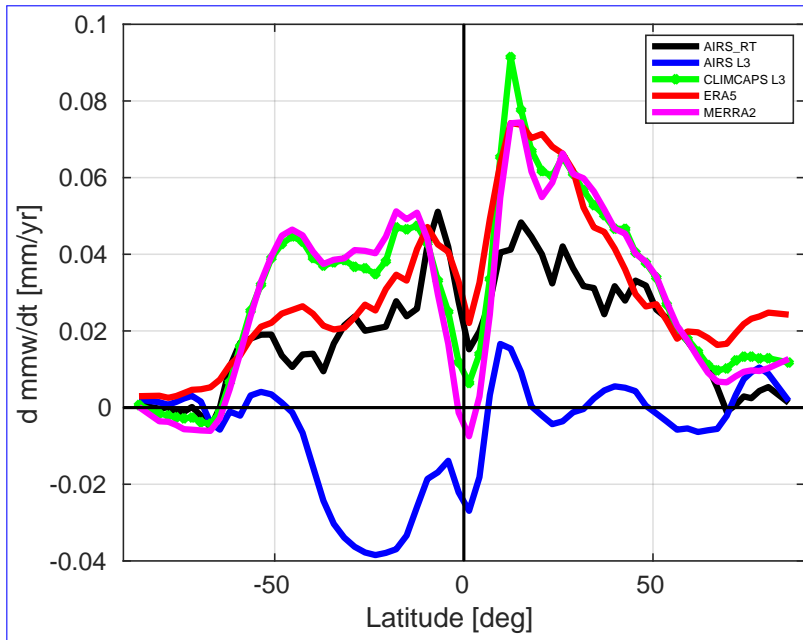


**Figure 10.** Zonally averaged column water vapor trends for AIRS\_RT, AIRS L3, CLIMCAPS L3, ERA5 and MERRA2.

937 ~~factor of 5.6 mentioned above will roughly equalize the  $y$ -axis of the two panels). The~~  
 938 ~~gray curve is the AIRS L1C observations, while the black curve is the reconstruction from~~  
 939 ~~the retrieval; the rest of the curves come from the fast model simulations using the relevant~~  
 940 ~~model/data fields. The error bars; not shown are the error bars which are on the order~~  
 941 ~~of  $\pm 0.005$  mm/year.~~

942 ~~The column water vapor trends for , AIRS L3, CLIMCAPS L3, ERA5 and MERRA2.~~  
 943 ~~The left hand panel shows the zonal averages, while the right hand panel shows the BT1231-BT1226~~  
 944 ~~zonally averaged trends.~~

945 ~~Close examination of the right hand panel AIRS\_RT is from our retrievals while~~  
 946 ~~the rest are directly from the NWP or L3 model fields. Close examination shows the CLIM-~~  
 947 ~~CAPS L3 column water trend is nearly identical to the MERRA2 trend, as is also seen~~  
 948 ~~in lower atmosphere water vapor trends shown later in Figure 13. Conversely the col-~~  
 949 ~~umn water vapor trends for AIRS L3 are negative in the lower troposphere in the mid-~~  
 950 ~~latitudes and tropics, which is not to be expected given that the surface temperature trends~~  
 951 ~~are positive. AIRS\_RT nominally agrees with ERA5 and MERRA2 in the tropics and~~  
 952 ~~midlatitudes, but is smaller than either in the northern polar regions. A reduced rate~~  
 953 ~~for AIRS\_RT is additionally seen in the 0-50 N latitudes, where there is a larger fraction~~  
 954 ~~of land (for which we do not use the assumption of constant relative humidity) compared~~  
 955 ~~to the Southern Hemisphere. Screening out the tiles over land slightly improves the agreement~~  
 956 ~~between reanalysis (ERA5, MERRA2) vs AIRS\_RT column water trends. Examination~~  
 957 ~~of the spectral trends in the window region does not shed any more insight into the differences,~~  
 958 ~~as the observation spectral trends and NWP reconstructed trends are very similar and~~  
 959 ~~we are fitting the observed trends. The magnitudes and patterns look similar to the 2005-~~  
 960 ~~2021 column water trends shown in Borger et al. (2022), which were derived using ob-~~  
 961 ~~servations from the Ozone Monitoring Instrument (OMI). We point out their 16 year zon-~~  
 962 ~~ally averaged trends look similar to the 20 year ERA5 zonally averaged column water~~  
 963 ~~trends between  $-60^{\circ}$ S and  $-10^{\circ}$ S, but become almost a factor of 2 larger between  $-10^{\circ}$ S~~

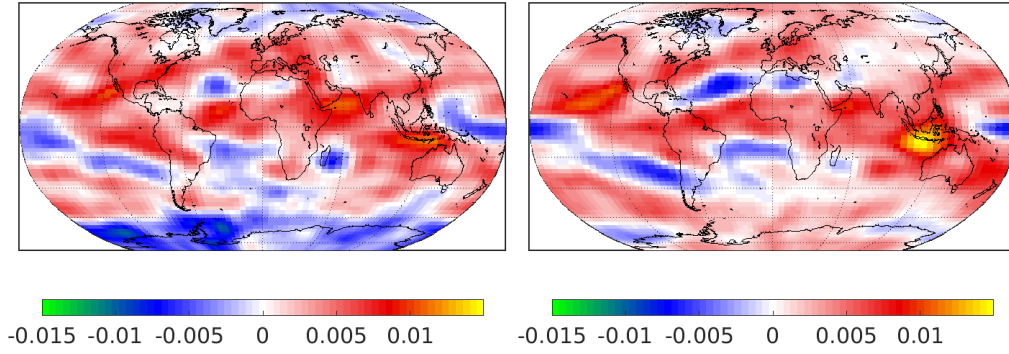


**Figure 11.** The 400 mb fractional water vapor trends for (left) AIRS\_RT and (right) ERA5 show general agreement except in the Southern Polar Regions.

964 and +40°N; the zonally averaged OMI 16 year trends are negative in the polar regions.  
 965 The column water trends are summarized in Table 4.

DATASET mm /year-yr <sup>-1</sup>	OMI 16 years	AIRS_RT 20 years	ERA5 20 years	MERRA2 20 years	AIRS 20 years
with MLS GLOBAL (cosine average)	0.051	<del>0.021</del> 0.021	0.035	0.036	-0.00
TROPICAL	0.083	<del>0.028</del> 0.028	0.047	0.042	-0.01

no MLS GLOBAL (cosine average) 0.029 TROPICAL 0.039

**Table 4.** Column water trends based on OMI data (16 years) and AIRS\_RT, ERA5 and MERRA2 (20 years). The units are in mm /year-yr<sup>-1</sup>; the uncertainties are on the order of 0.1 mm /year-yr<sup>-1</sup> for OMI and AIRS\_RT, and half that for ERA5 and MERRA2, and AIRS L3 and CLIMCAPS L3. trends using MLS a-priori are shown in the table, as are trends without the MLS a-priori

966 D/N differences (not shown) for AIRS\_RT were on the order of  $\pm 0.005$  mm /year-yr<sup>-1</sup>  
 967 yr<sup>-1</sup> (with daytime trends being smaller over land), for AIRS L3 were on the order of  
 968  $\pm 0.01$  mm /year-yr<sup>-1</sup> or more (with larger values happening over the daytime tropical  
 969 oceans), while that for ERA5 and CLIMCAPS L3 were typically on the order of  $\pm$   
 970 0.03 mm /year-yr<sup>-1</sup> or less. Figure 11 shows the 400 mb fractional water vapor trends,  
 971 with the left panel being the AIRS\_RT trends while the right panel is the ERA5 trends.  
 972 Note that there is general agreement except in the Southern Polar region, which is as  
 973 also seen later in Figure 13 to some extent in the other two observational L3 datasets  
 974 (AIRS v3 and CLIMCAPS). This could be related to a paper work by Boisvert et al. (2019)  
 975 who showed decreasing evaporation from the Southern Ocean in the 2003-2016 period  
 976 due to increasing ice cover.

977

#### 978 7.4 Zonal atmospheric temperature and water vapor trends

979

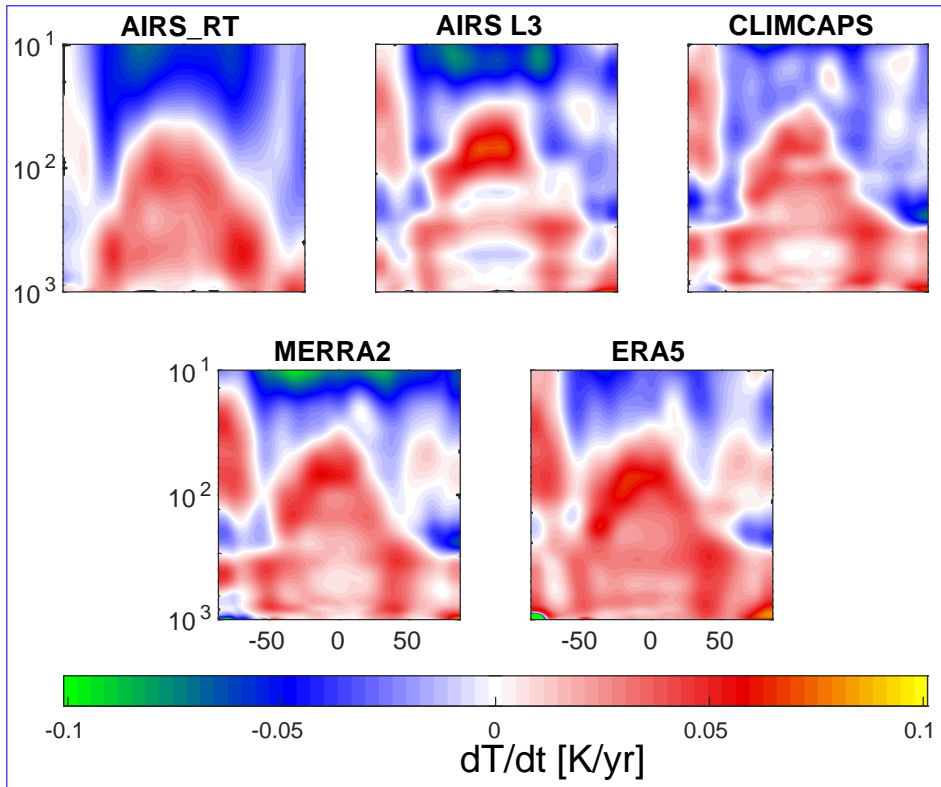


**Figure 12.** Zonally averaged  $dT/dt$  shown in 5 panels. Horizontal axis is latitude while vertical axis is pressure. The  $y$ -limits are between 10 to 1000 mb, on a logarithmic scale.

980 Figure 12 shows the zonally averaged atmospheric temperature trends from five of  
 981 the datasets in Figures 7,10 above. In the troposphere the AIRS\_RT retrievals show the  
 982 same general features as the trends from ERA5, though they begin to diverge in the strato-  
 983 sphere and especially above that. In particular AIRS\_RT does not show warming in the  
 984 Southern Polar stratosphere; we have separately looked into seasonal trends and noted  
 985 that our retrieved September/October/November temperature trends in the upper at-  
 986 mospheric Southern Polar regions are on the order of  $-0.12\text{K year}^{-1}$ , possibly lead-  
 987 ing to an overall no net heating/cooling for the annual trends. In addition we point out  
 988 that both our results and AIRS v7 L3 show a hint of cooling over the tropical surfaces.  
 989 Note that CLIMCAPS is initialized by MERRA2, and their temperature trends are quite  
 990 similar. AIRS v7 looks similar to AIRS\_RT except in the tropics where it almost has  
 991 cooling in the lower troposphere and much more warming in the lower stratosphere. The  
 992 correlations between AIRS\_RT and the [AIRS L3, CLIMCAPS L3, MERRA2, ERA5]  
 993 temperature trends of Figure 12 are [0.74,0.65,0.74,0.72] respectively.

994

995 Figure 13 shows the zonally averaged atmospheric fractional water vapor trends  
 996 ( $d/dt \text{ WV}(z,t)/\langle \text{WV}(z,t) \rangle$ ). The five panels are markedly different from one another.  
 997 The AIRS\_RT trends resemble those of ERA5 in the tropical troposphere, though we  
 998 do not have drying in the lower tropical layers. Conversely, the observed trends in the  
 999 Southern Polar (AIRS L3, CLIMCAPS L3 and AIRS\_RT) show drying rather than wet-  
 1000 ting, though AIRS\_RT is less than that of CLIMCAPS/MERRA2. AIRS\_RT is an out-  
 1001 lier in the upper polar atmosphere trends, as both the signals and the jacobians are close  
 1002 to zero. Of some concern is a little bit of drying in the northern polar region, where there

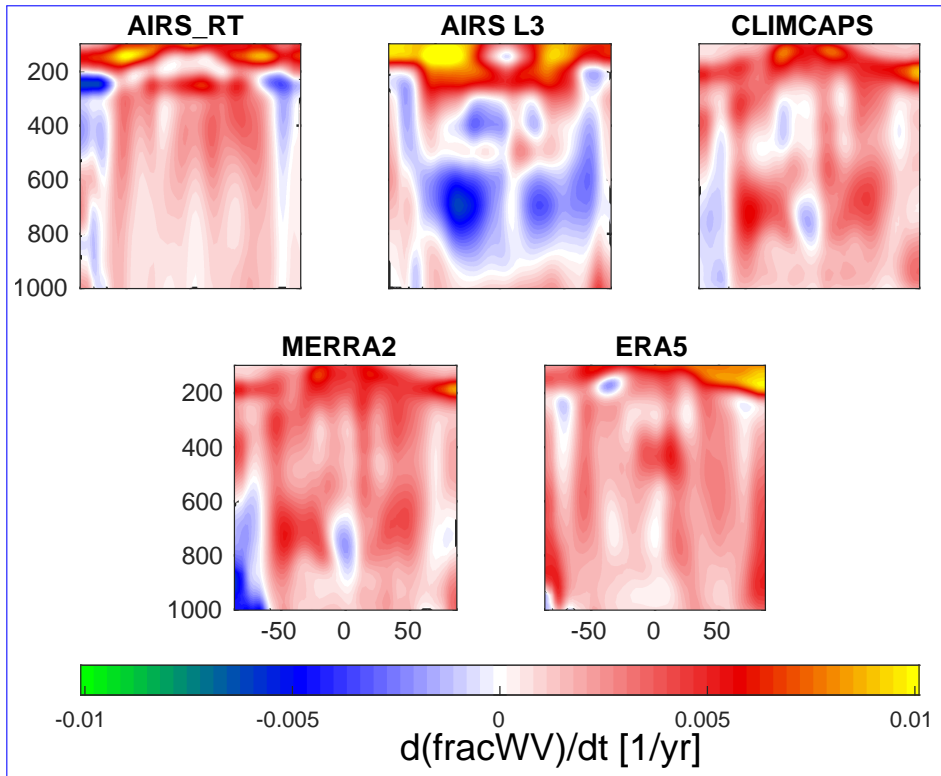


**Figure 13.** Zonally averaged  $d\text{WVfrac}/dt$  shown in 5 panels. Horizontal axis is latitude while vertical axis is pressure. The  $y$ -limits are between 100 to 1000 mb, on a linear scale.

1003 are low  $\text{H}_2\text{O}$  amounts leading to small jacobians. CLIMCAPS v2 looks quite similar to  
 1004 the MERRA2 trends. AIRSv7 shows substantial drying in the lower troposphere, and  
 1005 considerable wetting in the upper troposphere, compared to any of the other datasets.  
 1006 Spectral closure studies (using the AIRS v7  $\text{H}_2\text{O}$  trend  $\times$  the  $\text{H}_2\text{O}$  jacobians derived above  
 1007 from ERA5 average profiles) are not shown here, but differ noticeably from the CCR trends  
 1008 from AIRS v7 in the  $1300\text{-}1600\text{ cm}^{-1}$  region, indicating there are inadequacies in the AIRS  
 1009 V7 water vapor retrievals. The correlations between AIRS\_RT and the [AIRS L3, CLIM-  
 1010 CAPS L3, MERRA2, ERA5] fractional water vapor trends of Figure 13 (limited to 100  
 1011 mb, 1000 mb) are [0.65,0.24,0.36,0.58] respectively.

## 1012 **7.5 Addition of Microwave Limb Sounder Water Vapor A-priori**

1013 ~~The Microwave Limb Sounder (MLS), on board NASA's Aura platform, is designed~~  
 1014 ~~for sounding of the atmosphere above 300 mb. We computed water vapor trends from~~  
 1015 ~~the L3 data produced for that instrument (above 300 mb) and used them as an for the~~  
 1016 ~~retrieval.~~

1017  ~~$d\text{WVfrac}/dt$  (left) without and (right) with MLS in the upper atmosphere~~

1018 ~~Figure 9 shows the retrieved fractional water vapor trends when the trend in the~~  
 1019 ~~upper atmosphere in the left and right panels were zero, or used MLS trends, respectively.~~  
 1020 ~~One sees that the additional information brought in by the instrument sensitive to upper~~  
 1021 ~~troposphere humidity, significantly changes the water vapor sounding especially in the~~  
 1022 ~~polar region by moving towards the MERRA2 and ERA5 fractional water vapor trends~~  
 1023 ~~seen in Figure 13.~~

## 1024 8 Uncertainty

1025 The uncertainties for the AIRS v7 geophysical products are impacted by radiance  
 1026 noise amplification due to cloud clearing Susskind et al. (2003) and the neural net first  
 1027 guess, while state vector errors are estimated based on regressions. CLIMCAPS L2 geo-  
 1028 physical products are similarly impacted by cloud clearing noise in the radiances, but  
 1029 these are fully propagated together with geophysical error estimates from the MERRA2  
 1030 first guess, through the retrieval algorithm which uses Optimal Estimation Smith and  
 1031 Barnett (2020). No estimate of uncertainties are available for the monthly L3 products.  
 1032

1033 The uncertainties for the AIRS\_RT trends is much more straightforward : the spec-  
 1034 tral uncertainties shown in Figure 4 are used together with the state vector covariance  
 1035 matrices to generate the uncertainty matrix using the relevant equations of Optimal Es-  
 1036 timation (Rodgers, 2000); we use the diagonal elements for the final uncertainties. Pan-  
 1037 els (A) and (C) of Figure 14 shows the zonally averaged (D/N) uncertainties as a func-  
 1038 tion of pressure and latitude. Inspection of the radiance trends uncertainties shown in  
 1039 the center panel of Figure 4 shows the upper atmosphere temperature sounding region  
 1040 ( $650\text{-}700\text{ cm}^{-1}$ ) has much larger uncertainty in the polar regions. The instrument and  
 1041 spectroscopy characteristics, coupled with these observational uncertainties, are such that  
 1042 for temperature the smallest errors are in the tropics while the largest errors are in pol-  
 1043 ar upper atmosphere, which are the regions below 100 mb where the ERA5 trends dif-  
 1044 fer most from AIRS\_RT trends. Similarly for water vapor the larger errors are in the  
 1045 lower atmosphere and above about 300 mb; the constant RH assumption and MLS *a-*  
 1046 *priori* help alleviate the errors.

1047 The  ~~$h = ztest(trend, \mu=0, trend\text{-}uncertainty)$~~  Z-test confirmed this picture, as seen  
 1048 in panels (B) and (D) of Figure 4, which show the temperature and fractional water  
 1049 vapor trends, together with black dots marking the (latitude, altitude) points where the  
 1050 ~~zero trend null hypothesis at the default significance level of trends are larger than the~~  
 1051 uncertainty in the trends, at the 5% was rejected significance level. This happens in panel  
 1052 (B) for the temperature trends in most of the tropical/mid-latitude free troposphere (and  
 1053 stratosphere) but not at the southern polar stratosphere; and in panel (D) for fractional  
 1054 water vapor trends in the 200-600 mb range, from the Southern Polar region to about  
 1055 +60 N latitude, and some spots in the Northern Polar.

## 1056 9 Discussion

1057 In general for surface temperature trends, the disagreements between the six sets  
 1058 shown in Figure 7 are over the polar regions and over land (especially over the Amazon  
 1059 and Central Africa) and are smallest over tropical and mid-latitude oceans, indicating  
 1060 the best agreements, except for slightly larger differences off the western coast of the Amer-  
 1061 icas and Africa (which have a prevalence of MBL clouds). The atmospheric temperature  
 1062 trends in general agreed except for the upper atmosphere polar regions and in the high  
 1063 altitudes (less than about 200 mb). Similarly fractional water vapor trends differed most  
 1064 in the upper atmosphere (200 mb and above) and in the tropical/mid-latitude 600-800  
 1065 mb region. A quick glance at Figure 13 shows the former is due to lower sensitivity to  
 1066 upper atmosphere water vapor, leading the AIRS\_RT retrievals to have low values while  
 1067 the AIRS L2 retrieval is initialized by a neural net; conversely the latter is due to the  
 1068 AIRS L3 retrieval being negative while the rest were mainly positive. Similarly the AIRS\_RT  
 1069 retrieval differs above the Antarctic continent.  
 1070

1071 In general the observed surface temperature trends from the AIRS\_RT retrievals  
 1072 agree with the ERA5 and MERRA2 trends, as well as the NASA GISS trends, except

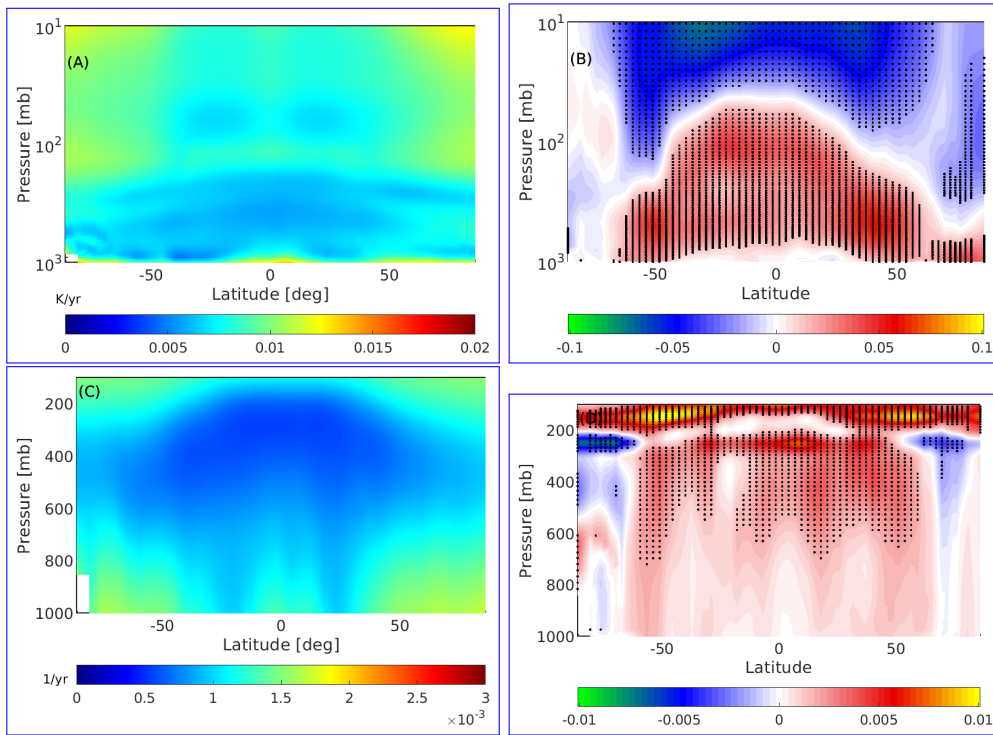


**Figure 14.** Zonally averaged D/N plots of (A) temperature uncertainties in  $\text{K/yr}^{-1}$  and (B) temperature trends in  $\text{K/yr}^{-1}$  together with null hypothesis. (C) and (D) are the same except for fractional water vapor uncertainty and trends in  $1/\text{year}$ . See text for more detailed explanation.

1073 in the Southern Antarctic. That is a region where there are few surface observations; for  
 1074 retrievals there are competing effects of using ice vs ocean surface emissivity. Overall,  
 1075 the AIRS\_RT retrieved surface temperature trends are typically in between ERA5 and  
 1076 MERRA2 for land + ocean in all regimes (tropical, midlatitude and polar), though slightly  
 1077 larger overall for ocean than the two reanalysis datasets; in general they are closer to the  
 1078 ERA5 trends than the MERRA2 trends.

1079 Strow et al. (2021) demonstrated that the long- and medium- wave channels of the  
 1080 AIRS instrument are radiometrically stable to better than 0.002-0.003 K  $/\text{yearyr}^{-1}$ , which  
 1081 is much smaller than the surface and tropospheric temperature trends in the reanaly-  
 1082 sis models, AIRS L3 data and our retrieved trends. After a separate analysis of spectral  
 1083 trend uncertainties after 05,10,15,20 years of observations, Figure ?? shows the trend spectral  
 1084 uncertainties years (not shown here) show that these uncertainties have been steadily  
 1085 decreasing and are now approaching this number, as can be seen in the bottom left panel  
 1086 of Figure 3. Furthermore, though we cannot guarantee only cloud free scenes in our cho-  
 1087 sen Q0.90 dataset used in this paper, the high correlations between other dataset sur-  
 1088 face trends compared to ours, is a good indication that our results come from mostly cloud-  
 1089 free scenes, or scenes whose clouds have negligible impact on our results.

1090 The observed zonal temperature trends agree with those from the models and the  
 1091 AIRS L3 products, except in the polar regions. Again this could be an issue of using slightly  
 1092 incorrect surface emissivity for the AIRS\_RT retrievals. In addition we point out that  
 1093 since there is very little water vapor, the temperature jacobians near the surface are quite  
 1094 small in magnitude (compared to more humid atmospheres) and so it is difficult to sep-  
 1095 arate out the effects of surface temperature trends versus lower atmosphere temperature  
 1096 and H<sub>2</sub>O trends. The quantile construction used in this paper means that for example  
 1097 tiles straddling the subcontinent of India and the ocean will preferentially pick the land  
 1098 surface observations for daytime, which could lead to misleading trends on these coastal  
 1099 tiles. It is possible to subdivide the  $3^\circ \times 5^\circ$  tiles into for example  $1^\circ \times 1^\circ$  grids and do the  
 1100 analysis, but the number of observations per small grid cell would drop, leading to more  
 1101 noise in the retrieved trend.

1102 The AIRS\_RT retrieved absolute column water trends are equal to/slightly larger  
 1103 than ERA5/MERRA2 in the tropics and below both of them in the midlatitudes; AIRS\_RT  
 1104 ocean column water trends were slightly smaller than both ERA5 and MERRA2 over  
 1105 ocean, and in-between them over land. We note the difficulties we have retrieving H<sub>2</sub>O  
 1106 close to the surface and in the upper atmosphere. This is simply a consequence of the  
 1107 sensitivity of the infrared sounder, namely most of the averaging kernels peak in the 300-  
 1108 600 mb range. AIRS\_RT column water trends agree with those from ERA5 and MERRA2  
 1109 column water trends in the tropics; nevertheless even with expected lowered sensitivity  
 1110 to water vapor in the lower altitudes, we were able to retrieve similar column water va-  
 1111 por trends to the NWP models both in the tropics and in the mid-latitudes. The dif-  
 1112 ferences become more acute in the polar regions since the low average amounts of wa-  
 1113 ter vapor mean the water vapor jacobians are very small, as were the observed trends  
 1114 in the WV channels. However, we point out that our column water trends, which are both  
 1115 quite sensitive to water vapor in the lower atmosphere, are in good agreement with those  
 1116 from NWP models.

1117 We point our here that our results are relatively robust to changes in the covari-  
 1118 ance or Tikonov parameter settings. For instance changing them by factors of two would  
 1119 keep the trends about the same, though of course the uncertainties would change.

1120 Given the complex numerical algorithms used in both the reanalysis models and  
 1121 the AIRS L3 retrievals as well as those in the AIRS\_RT trends, it is difficult to offer pre-  
 1122 cise explanations for any of the trends shown above. There are however a few general  
 1123 points that can be made. The first is that since infrared instruments are sensitive to the  
 1124 300-800 mb region and lose sensitivity outside this, the retrievals from AIRS\_RT and

1125 AIRS L3 have difficulties with water vapor in the lower (Planetary Boundary Layer) and  
 1126 upper troposphere/lower stratosphere. One way to mitigate this is to use trended data  
 1127 from external sources ~~;~~for in the *a-priori*, while keeping the *a-priori*trends for all other  
 1128 parameters as 0. For example we have shown we can use the MLS data above 300 mb  
 1129 without significantly degrading the AIRS\_RT retrieval in the middle and lower atmo-  
 1130 sphere; conversely the CLIMCAPS retrievals are initialized by MERRA2 and while they  
 1131 can pull out weather signals, their L3 trends are still quite closely tied to the MERRA2  
 1132 trends. The tropical and mid-latitude ocean surface temperature trends from the numer-  
 1133 ical models that assimilate data, L3 products and AIRS\_RT are very similar; however  
 1134 they start to show differences where there are few *in-situ* data combined with problems  
 1135 with ice identification (surface emissivity)/cold temperatures which exacerbate the drift-  
 1136 ing AIRS detector problems Strow et al. (2021), such as the Arctic and Southern Ocean.

## 1137 10 Conclusions

1138 We have described a novel method to obtain global thermodynamic atmospheric  
 1139 climate trends, starting from infrared allsky hyperspectral observations which are then  
 1140 subset for “nominally clear” scenes. Our retrieved trends are derived using trends from  
 1141 well characterized (radiometrically stable) radiances and from zero *a-priori* (except for  
 1142 a constant relative humidity assumption). This makes them much more direct and trace-  
 1143 able than trends from traditional L2 retrieval algorithms, which use complicated *a-priori*  
 1144 information. We also did “radiative closure” tests by running the monthly NWP or L3  
 1145 fields through a radiative transfer model to compare the spectral trends so obtained against  
 1146 the observed spectral trends, which showed the most disagreement in the water vapor  
 1147 sounding regions.

1148 The temperature and water vapor trends retrieved from the “nominally clear” ra-  
 1149 diance trends resemble those computed from monthly ERA5 and MERRA2 reanalysis.  
 1150 The radiative spectral closure helps identify the cause of differences in the geophysical  
 1151 trends, rather than solely attributing them to deficiencies (eg the well known reduced  
 1152 sensitivity to water vapor near the boundary layer and above 200 mb) with our retrieval.  
 1153 For example the AIRS\_RT temperature trends are quite similar to the reanalysis (MERRA2/ERA5)  
 1154 trends, while the water vapor (and/or Relative Humidity) trends are quite different, es-  
 1155 pecially in the lower troposphere and upper troposphere, which is clearly manifest as dif-  
 1156 ferences in the spectral trends in the water vapor sounding region.

1157 The 20 years of AIRS observations were binned into nominal  $3 \times 5$  degree grid boxes  
 1158 covering the planet, with a time step of 16 days, from which anomalies and trends were  
 1159 obtained. To alleviate the reduced sensitivity of hyperspectral sounders to water vapor  
 1160 in the lower atmosphere we used an assumption of 0.01 increase in relative humidity to  
 1161 initialize the *a-priori* lower atmosphere fractional water vapor rates, while we similarly  
 1162 used Microwave Limb Sounder trends as an *a-priori* to address the high altitude water  
 1163 vapor deficiencies caused by lower sensitivity to upper atmosphere water vapor. New or  
 1164 updated time dependent surface emissivity databases may become available in the fu-  
 1165 ture, enabling us to include those effects into Equation 4. Problems in the polar regions  
 1166 and Planetary Boundary Layer water vapor retrievals will be harder to overcome since  
 1167 there is very little sensitivity to water vapor in these regions, together with fewer obser-  
 1168 vations to compare against, though more work is planned to address both of these.

1169 In this paper we used the 90th quantile (Q0.90) nominally “hottest” observed BT1231  
 1170 data to form a time series over which to obtain radiance trends, after establishing that  
 1171 the spectral trends from this quantile differed by less than about  $\pm 0.0015 \text{ K } \text{yr}^{-1}$   
 1172 from the 50th (or average) quantile. In the future we plan to base the data subset se-  
 1173 lection on MODIS cloud products (obtained at 1 km resolution compared to the AIRS  
 1174 15 km resolution). In any case the AIRS L1C Q0.90 spectral trends used for the AIRS\_RT  
 1175 results are very comparable to trends from quality assured binned AIRS CCR data Manning



1176 (2022). The quantile method allows us to select which data to use in the trends : we have  
 1177 explored doing the trend retrievals using the cloud fields contained in ERA5, together  
 1178 with the TwoSlab cloud algorithm De Souza-Machado et al. (2018) to compute jacobians  
 1179 when clouds are present, together with trends from the Q0.50 dataset described above.  
 1180 The retrieved geophysical trends resemble those described above in the mid to upper at-  
 1181 mosphere, and differ in the lower atmosphere, but more work is needed on this and is  
 1182 not discussed further. Longwave clear sky flux trends (both outgoing top-of-atmosphere  
 1183 and incoming bottom-of-atmosphere) and climate feedbacks will be discussed in a sep-  
 1184 arate paper.

1185 While the Aqua platform is scheduled to be terminated within the next few years,  
 1186 copies of near identical CrIS instruments are already in orbit, and more will be launched  
 1187 over the next few years, till at least 2040. The Climate Hyperspectral Infrared Radiance  
 1188 Product (CHIRP) Strow et al. (2021) will seamlessly combine the AIRS data between  
 1189 2002-2015 to CrIS data from 2015-2040 to obtain a 40 year observational radiance record  
 1190 over which to study climate. This availability means that AIRS\_RT and future AIRS/CrIS  
 1191 versions, is well positioned to enable climate analysis of geophysical trends for years to  
 1192 come.

## 1193 **Appendix A Day versus Night surface temperature trend differences**

1194 Figure A1 shows the (top) daytime and (middle) nighttime surface temperature  
 1195 trends; from left to right the datasets are (observational) AIRS\_RT, AIRS L3, CLIM-  
 1196 CAPS L3 and (reanalysis) ERA5. In general the AIRS observational datasets show en-  
 1197 hanced daytime cooling over the Indian subcontinent and Central Africa, compared to  
 1198 the ERA5 model; they also show daytime warming trends over continental Europe and  
 1199 central Asia and the Amazon are larger than during the nighttime. With the large ocean  
 1200 heat capacity and smaller land heat capacity, the land is expected to show more of a di-  
 1201 urnal cycle than ocean. ERA5 sees warming over Eastern/Central Africa during daytime  
 1202 while the observational datasets see cooling. Similarly the three observational datasets  
 1203 see more daytime cooling over the Indian sub-continent and south eastern Australia than  
 1204 does ERA5; we omit more detailed analysis in this paper. During the nighttime, the AIRS  
 1205 L3 product has cooling over C. Africa and parts of the Amazon. The day-night differ-  
 1206 ences are seen in the bottom row of the same figure. Note the colorbar is the same for  
 1207 all three rows. The differences are close to zero over the ocean. AIRS\_RT and CLIM-  
 1208 CAPS L3 see more daytime cooling over E. Africa and the Indian subcontinent. Over-  
 1209 all the magnitude of the day - night differences for the observations are larger for the AIRS  
 1210 observational datasets than for ERA5. ERA5 also sees negative differences over Central  
 1211 Asia compared to the AIRS observational datasets, which see positive differences (higher  
 1212 surface temperature trends during the daytime).

1213

1214 The atmospheric temperature and fractional water vapor day-night differences are  
 1215 quite small (compared to the average values) and not shown here; AIRS L3 shows no-  
 1216 ticeable more wetting of the 600-800 mb region during daytime versus nighttime, com-  
 1217 pared to the other three.

## 1218 **Data availability** [Open Research Section](#)

1219 The AIRS L3 and CLIMCAPS L3 data products, as well as the AIRS L1C radi-  
 1220 ances are freely available to the public on the NASA servers. MERRA2 and ERA5 and  
 1221 GISTEMP model output are also freely available.

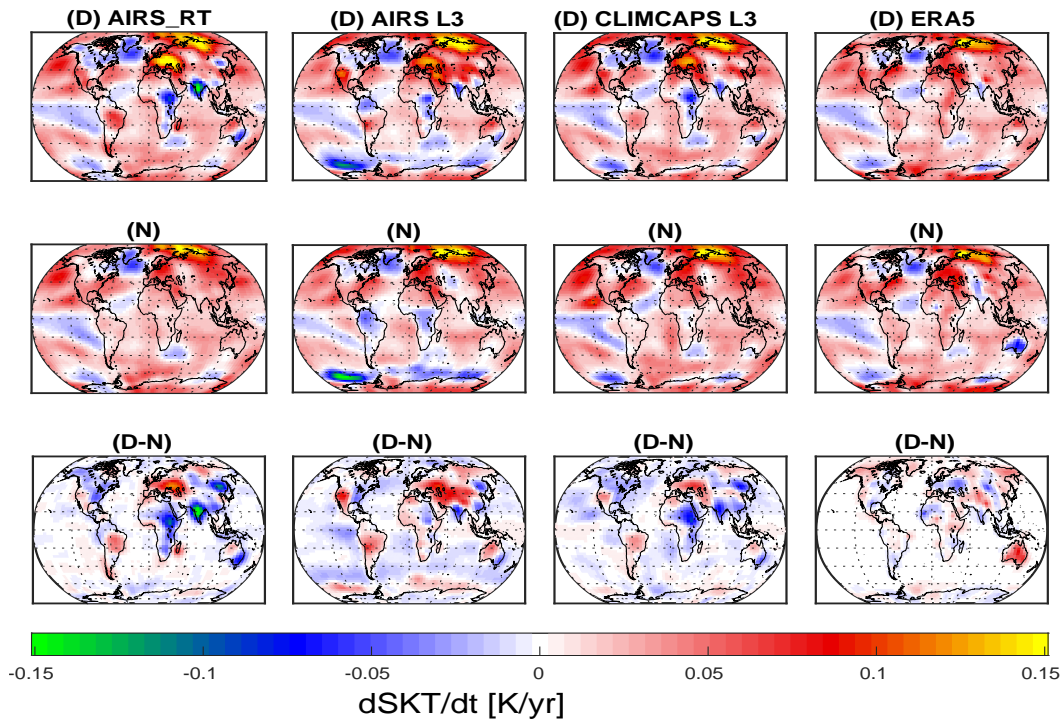


**Figure A1.** Top two rows : The (top) day and (middle) night surface temperature trends for AIRS\_RT, AIRS L3, CLIMCAPS L3 and ERA5. Third row (bottom) is the D-N difference.

### 1222 **Author contribution**

1223 ~~Sergio DeSouza-Machado prepared the manuscript with contributions from all co-authors,~~  
 1224 ~~and did most of the data analysis in this manuscript. L. Strow envisaged the concept~~  
 1225 ~~of tiling the AIRS observations into tiles and drove the research work. R. Kramer provided~~  
 1226 ~~valuable advice regarding the methods and data analysis, as well in preparing the manuscript.~~  
 1227

### 1228 **Competing interests**

1229 ~~The authors declare that they have no conflict of interest.~~

### 1230 **Acknowledgments**

1231 We gratefully acknowledge the help of H. Motteler, who designed, implemented and  
 1232 ran the AIRS tiling code. C. Hepplewhite helped test the outputs of the tiling code, S.  
 1233 Buczkowski worked on bringing down almost all the data used in this study, and made  
 1234 the uniform/clear datasets. Chris Barnett has given helpful comments and general ad-  
 1235 vice regarding retrievals and comparisons to the AIRSv7 and CLIMCAPS datasets. The  
 1236 hardware used is part of the UMBC High Performance Computing Facility (HPCF). The  
 1237 facility is supported by the U.S. National Science Foundation through the MRI program  
 1238 (grant nos. CNS-0821258, CNS-1228778, OAC-1726023, and CNS-1920079) and the  
 1239 SCREMS program (grant no. DMS-0821311), with additional substantial support from  
 1240 the University of Maryland, Baltimore County (UMBC). See [hpcf.umbc.edu](http://hpcf.umbc.edu) for more  
 1241 information on HPCF and the projects using its resources.

1242

**References**

1243

2023, G. T. (2005). *GISS Surface Temperature Analysis (GISTEMP), version 4* (Tech. Rep.). data accessed 2023/11/30 at <https://data.giss.nasa.gov/gistemp/>: NASA Goddard Institute for Space Studies.

1244

1245

1246

Boisvert, L., Vihma, T., & Shie, C.-L. (2019). Evaporation From the Southern Ocean Estimated on the Basis of AIRS Satellite Data. *JGR*, *125*, <https://doi.org/10.1029/2019JD030845>.

1247

1248

1249

1250

1251

1252

Borbas, E., Hulley, G., Feltz, M., Knuteson, R., & Hook, S. (2018). The Combined ASTER MODIS Emissivity over Land (CAMEL) Part 1: Methodology and High Spectral Resolution Application. *Remote Sens.*, *10*, 643; <https://doi.org/10.3390/rs10040643>.

1253

1254

1255

1256

Borger, C., Beirle, S., & Wagner, T. (2022). Analysis of global trends of total column water vapour from multiple years of OMI observations. *Atmos. Chem. Phys.*, *22*, 10603–10621, <https://doi.org/10.5194/acp-22-10603-2022>.

1257

1258

1259

Clough, S., Shephard, M., Mlawer, E., Delamere, J., Iacono, M. J., Cady-Pereira, K., ... Brown, P. (2005). Atmospheric radiative transfer modeling : a summary of the AER codes. *J. Quant. Spectrosc. Rad. Trans.*, *91*, 233–244; [doi:10.1016/j.qsrtr.2004.05.058](https://doi.org/10.1016/j.qsrtr.2004.05.058).

1260

1261

1262

1263

De Souza-Machado, S., Strow, L. L., Motteler, H., & Hannon, S. (2020). kCARTA : A Fast Pseudo Line by Line Radiative Transfer Algorithm with Analytic Jacobians, Fluxes, Non-Local Thermodynamic Equilibrium and Scattering. *Atmos. Meas. Tech.*, *31*, 323–339, <https://doi.org/10.5194/amt-13-323-2020>.

1264

1265

1266

1267

De Souza-Machado, S., Strow, L. L., Tangborn, A., Huang, X., Chen, X., Liu, X., ... Yang, Q. (2018). Single-footprint retrievals for AIRS using a fast TwoSlab cloud-representation model and the SARTA all-sky infrared radiative transfer algorithm. *Atmos. Meas. Tech.*, *11*, 529–550, <https://doi.org/10.5194/amt-11-529-2018>.

1268

1269

1270

1271

Gelaro, R., & Coauthors. (2017). MERRA-2 Overview: The Modern-Era Retrospective Analysis for Research and Applications, Version 2 (MERRA-2). *J. Clim.*, *30*, 5419–5454, [doi: 10.1175/JCLI-D-16-0758.1](https://doi.org/10.1175/JCLI-D-16-0758.1).

1272

1273

1274

Gordon, I., & Rothman, L. e. a. (2022). The HITRAN 2020 molecular spectroscopic database. *J. Quant. Spectrosc. Rad. Trans.*, *277*, 1–82, <https://doi.org/10.1016/j.jqsrt.2021.107949>.

1275

1276

Haiden, T., Dahoui, M., Ingleby, B., de Rosnay, P., Prates, C., Kuscü, E., ... Jones, L. (2018). *Use of in situ surface observations at ECMWF* (No. 834).

1277

1278

1279

Hersbach, H., Bell, B., Berrisford, P., Hirahara, S., Horányi, A., Muñoz-Sabater, J., ... Thépaut, J.-N. (2020). The ERA5 Global Reanalysis. *Quart. J. Roy. Meteorol. Soc.*, *146*, 1999–2049, <https://doi.org/10.1002/qj.3803>.

1280

1281

1282

Huang, X., Chen, X., Fan, X., Kato, S., Loeb, N., Bosilovich, M., ... Strow, L. (2023). A Synopsis of AIRS Global-Mean Clear-Sky Radiance Trends From 2003 to 2020. *JGR*, *127*, e2022JD037598, <https://doi.org/10.1029/2022JD037598>.

1283

1284

1285

1286

Irion, F., Kahn, B., Schreier, M., Fetzner, E., Fishbein, E., Fu, D., ... Yue, Q. (2018). Single-footprint retrievals of temperature, water vapor and cloud properties from AIRS. *Atmos. Meas. Tech.*, *11*(2), <https://doi.org/10.5194/amt-11-971-2018>.

1287

1288

1289

1290

King, M., Platnick, S., Menzel, P., Ackerman, S., & Hubanks, P. (2013). Spatial and Temporal Distribution of Clouds Observed by MODIS Onboard the Terra and Aqua Satellite. *IEEE*, *51*, 3826–3852, [10.1109/TGRS.2012.2227333](https://doi.org/10.1109/TGRS.2012.2227333).

1291

1292

1293

1294

Lambert, A., Read, W., Livesey, N., & Fuller, R. (2021). *MLS/Aura Level 3 Monthly Binned Vapor (H<sub>2</sub>O) Mixing Ratio on Assorted Grids V005* (Tech. Rep.). [https://disc.gsfc.nasa.gov/datasets/ML3MBH20\\_005/summary](https://disc.gsfc.nasa.gov/datasets/ML3MBH20_005/summary): NASA Greenbelt, MD, USA, Goddard Earth Sciences Data and Information Services Center (GES DISC).

1295

1296

Lenssen, N., Schmidt, G., Hansen, J., Menne, M., Persin, A., Ruedy, R., & Zys, D.

- 1297 (2019). Improvements in the GISTEMP uncertainty model. *JGR*, *124*(12),  
1298 6307-6326, doi:10.1029/2018JD029522.
- 1299 Lin, Y., & Oey, L. (2020). Global Trends of Sea Surface Gravity Wave, Wind, and  
1300 Coastal Wave Setup. *J. Clim.*, *33*, 769–785, <https://doi.org/10.1175/JCLI-D-19-0347.1>.  
1301
- 1302 Maddy, E., & Barnett, C. (2008). Vertical Resolution Estimates in Version 5 of  
1303 AIRS Operational Retrievals. *IEEE*, *66*(8), 2375-2384, DOI 10.1109/T-  
1304 GRS.2008.917498.
- 1305 Manning, E. (2022). *Nasa jpl private communication, 4/2022*. (AIRS CCR L3 data)
- 1306 Manning, E., Aumann, H., Broberg, S., Pagano, T., Wilosn, R., Yanovsky, I.,  
1307 & Strow, L. (2020). *Eos airs l1c data product user guide* (Tech. Rep.).  
1308 [https://docserver.gesdisc.eosdis.nasa.gov/public/project/AIRS/V6.7\\_L1C\\_Product\\_User\\_Guide.pdf](https://docserver.gesdisc.eosdis.nasa.gov/public/project/AIRS/V6.7_L1C_Product_User_Guide.pdf):  
1309 NASA.
- 1310 Masuda, K., Takashima, T., & Takayama, Y. (1988). Emissivity of pure and sea wa-  
1311 ters for the model sea surface in the infrared window regions. *Remote Sensing*  
1312 *of Environment*, *24*, 313–329.
- 1313 Palchetti, L., Brindley, H., Bantges, R., Buehler, S. A., Camy-Peyret, C., Carli, B.,  
1314 ... Serio, C. (2020). FORUM: unique far-infrared satellite observations to  
1315 better understand how Earth radiates energy to space. *Bull.Amer.Met.Soc.*,  
1316 *101*, <https://doi.org/10.1175/BAMS-D-19-0322.1>.
- 1317 Peters, W., Jacobson, A., Sweeney, C., & Tans, P. (2007). An atmospheric perspec-  
1318 tive on North American carbon dioxide exchange: CarbonTracker. *Proc. Nat.*  
1319 *Aca. Sci.*, *104*, 18925-18930, <https://doi.org/10.1073/pnas.0708986104>.
- 1320 Prakash, S., & Norouzi, H. (2020). Land surface temperature variability across In-  
1321 dia: a remote sensing satellite perspective. *Theor. Appl. Climatol.*, *139*, 773-  
1322 784, <https://doi.org/10.1007/s00704-019-03010-8>.
- 1323 Raghuraman, S., Paynter, D., V., R., & Menzel, R. H. X. (2023). Green-  
1324 house Gas Forcing and Climate Feedback Signatures Identified in Hy-  
1325 perspectral Infrared Satellite Observations. *Geophys. Res. Lett.*, *50*,  
1326 <https://doi.org/10.1029/2023GL103947>.
- 1327 Rodgers, C. (2000). Inverse Methods for Atmospheric Sounding. In (p. 256 pages).  
1328 World Scientific, Singapore.
- 1329 Roemer, F., Buehler, S., Brath, M., Kluft, L., & John, V. (2023). Direct observation  
1330 of Earth’s spectral long-wave feedback parameter. *Nature Geoscience*, *16*, 416-  
1331 421, <https://doi.org/10.1038/s41561-023-01175-6>.
- 1332 Sherwood, S., Ingram, W., Tshushuma, Y., Satoh, M., Roberts, M., Vidale, P., &  
1333 O’Gorman, P. (2010). Relative humidity changes in a warmer climate. *J.*  
1334 *Geophys. Res.*, *115*, <https://doi.org/10.1029/2009JD012585>.
- 1335 Smith, N., & Barnett, C. (2019). Uncertainty Characterization and Propa-  
1336 gation in the Community Long-Term Infrared Microwave Combined At-  
1337 mospheric Product System (CLIMCAPS). *Remote Sensing*, *11*, 1227-  
1338 1251, doi:10.3390/rs11101227.
- 1339 Smith, N., & Barnett, C. (2020). CLIMCAPS observing capability for temperature,  
1340 moisture, and trace gases from AIRS/AMSU and CrIS/ATMS. *AMT*, *13*,  
1341 4437–4459, <https://doi.org/10.5194/amt-13-4437-2020>.
- 1342 Smith, N., & Barnett, C. (2023). Practical Implications of CLIMCAPS Cloud  
1343 Clearing and Derived Quality Metrics. *Earth Space Sci*, *10*, e2023EA002913.  
1344 <https://doi.org/10.1029/2023EA002913>.
- 1345 Soden, B., & Held, I. (2006). An assessment of climate feedbacks in coupled ocean-  
1346 atmosphere models. *J. Clim*, *19*, 3354-3360.
- 1347 Strow, L., & DeSouza-Machado, S. (2020). Establishment of AIRS climate-level  
1348 radiometric stability using radiance anomaly retrievals of minor gases and sea  
1349 surface temperature. *Atmos. Meas. Tech.*, *13*, <https://doi.org/10.5194/amt-13-4619-2020>.  
1350
- 1351 Strow, L., Hannon, S., DeSouza-Machado, S., Tobin, D., & Motteler, H. (2003).

- 1352 An overview of the AIRS radiative transfer model. *IEEE Transactions on*  
1353 *Geosciences and Remote Sensing*, 41, 303-313.
- 1354 Strow, L., Hannon, S., Weiler, M., Overoye, K., Gaiser, S., & Aumann, H. (2003).  
1355 Pre-launch spectral calibration of the Atmospheric InfraRed Sounder (AIRS).  
1356 *IEEE Transactions on Geosciences and Remote Sensing*, 41, 274-286.
- 1357 Strow, L., Hepplewhite, C., Motteler, H., Buczkowski, S., & DeSouza-Machado, S.  
1358 (2021). A Climate Hyperspectral Infrared Radiance Product (CHIRP) Com-  
1359 bining the AIRS and CrIS Satellite Sounding Record. *Rem. Sens.*, 13(3),  
1360 <https://doi.org/10.3390/rs13030418>.
- 1361 Susskind, J., Barnet, C., & Blaisdell, J. (2003). Retrieval of atmospheric and sur-  
1362 face parameters from AIRS/AMSU/HSB data under cloudy conditions. *IEEE*  
1363 *Transactions on Geosciences and Remote Sensing*, 41, 390-409.
- 1364 Susskind, J., Blaisdell, J., & Iredell, L. (2014). Improved methodology for surface  
1365 and atmospheric soundings, error estimates, and quality control procedures:  
1366 the Atmospheric Infrared Sounder science team version-6 retrieval algorithm.  
1367 *J. App. Rem. Sens.*, 8(1), 084994 [10.1117/1.JRS.8.084994].
- 1368 Tian, B., E. M., Roman, J., Thrastarson, H., & Fetzer, R., E. ad Monarrexz.  
1369 (2020). *Airs version 7 level 3 product user guide* (Tech. Rep.). Jet  
1370 Propulsion Laboratory, California Institute of Technology. Retrieved from  
1371 [https://docserver.gesdisc.eosdis.nasa.gov/public/project/AIRS/](https://docserver.gesdisc.eosdis.nasa.gov/public/project/AIRS/V7_L3_User_Guide.pdf)  
1372 [V7\\_L3\\_User\\_Guide.pdf](https://docserver.gesdisc.eosdis.nasa.gov/public/project/AIRS/V7_L3_User_Guide.pdf)
- 1373 Whitburn, S., Clarisse, L., Bouilon, M., Safieddine, S., George, M., Dewitte, S.,  
1374 ... Clerbaux, C. (2021). Trends in spectrally resolved outgoing longwave  
1375 radiation from 10 years of satellite measurements. *npj Clim Atmos Sci*, 4,  
1376 48, <https://doi.org/10.1038/s41612-021-00205-7>.
- 1377 Wu, W., Liu, X., Lei, X., L. amd Xiong, Yang, Q., Yue, Q., Zhou, D., & Larar, A.  
1378 (2023). Single field-of-view sounder atmospheric product retrieval algorithm  
1379 : establishing radiometric consistency for hyper-spectral sounder retrievals.  
1380 *AMT*, 16, 4807-4832, <https://doi.org/10.5194/amt-16-4807-2023>.
- 1381 Zhou, D., Larar, A., Liu, X., Smith, W., Strow, L., Yang, P., ... Calbet, X. (2011).  
1382 Global Land Surface Emissivity Retrieved From Satellite Ultraspectral IR  
1383 Measurements. *IEEE Trans. Geosci. Remote Sens.*, 49(4), 1277-1290.